Received: 6 April 2023 | Revised: 10 January 2024 | Accepted: 15 April 2024

DOI: 10.1002/pip.3813

RESEARCH ARTICLE

PROGRESS IN PHOTOVOLTAICS WILEY

Practical design of an optical filter for thermal management of photovoltaic modules

Juan Camilo Ortiz Lizcano[1] | Ismail Kaaya[2] | Hesan Ziar[1] | Patricia Seoane da Silva[1] | Yilong Zhou[1] | Miro Zeman[1] | Olindo Isabella[1]

[1]Delft University of Technology, Delft, Netherlands

[2]Imec, Imo-Imomec, Genk, Belgium

Correspondence
Juan Camilo Ortiz Lizcano and Hesan Ziar, Delft University of Technology, Mekelweg 4, Delft 2628CD, Netherlands.
Email: j.c.ortizlizcano@tudelft.nl and h.ziar@tudelft.nl

Funding information
Horizon 2020 Program, Grant/Award Number: 952957

Abstract

This work presents a practical approach to designing an optical filter for thermal management for photovoltaic modules. The approach emphasizes the practicality of manufacturing over optical performance. Simulation work demonstrates that, for an interdigitated back contact solar cell architecture, complete rejection of infrared radiation offers limited thermal benefits requiring highly complex optical filter designs. An alternative approach consists of reducing thermalization losses by providing reflectance at lower wavelength values. An optical filter design that fulfills this requirement is possible using simple structures based on two materials and taking advantage of the harmonics present in quarter wavelength optical thickness designs. The filter is later optimized for angular performance via second-order algorithms, resulting in a device consisting of only 15 thin-film layers. Performance simulations on two locations, Delft (the Netherlands) and Singapore, estimate a temperature reduction of 2.20°C and 2.45°C, respectively. In a single year, the optical loss produced by the filter is not compensated via temperature reduction. However, improvements in the annual degradation rate show that in Singapore, the overall effect of the filter on the lifetime DC energy yield is positive.

KEYWORDS
lifetime, optical filters, performance modeling, reliability, thermal management

1 | INTRODUCTION

In recent years, research has been driving the efficiency of crystalline silicon (c-Si) solar cells to such an extent that it almost reaches its theoretical limit. There is, however, still room for improvement. The efficiency of a solar cell is highly dependent on its operational temperature. C-Si solar cells have temperature coefficients related to output power in the range of −0.3% to −0.4%.[1] If operating at 60°C, a c-Si solar cell that produces 4 W under standard test conditions (STC) can lose between 11% and 14% of its power due to its increased temperature.

Moreover, research suggests that the reliability of photovoltaic (PV) modules seems very sensitive to their operational temperature.[2–4] Modules that consistently perform at high temperatures throughout the year can have a significantly shortened lifespan. Improving reliability is instrumental in bolstering the economics of PV systems and is essential, more specifically, for building integrated photovoltaics (BIPV). A module installed on an integrated system usually presents a higher operational temperature than operating on a standard rack-mounted configuration.[5] Long lifetimes are required on BIPV modules so they can be competitive in this aspect with the building materials they are

replacing. Thus, thermal management is an increasingly important aspect of the design of PV modules.

Over the last decades, researchers have studied many options to reduce the operating temperatures of PV modules.[6–8] Though widely varied, the proposed solutions fall into two main categories: passive and active approaches.[9] Active approaches utilize auxiliary systems, usually to significantly improve convective cooling, and utilize the heat produced on the PV modules for other applications, such as residential or commercial water heating.[10] The active system provides more predictable cooling power than the passive approach but demands an external energy source.

Passive approaches rely on environmental factors (such as wind speed) or installation layouts (e.g., non-insulating PV module backside) to provide observable benefits.[6] A passive approach utilizes devices that take advantage of physical principles that can increase cooling effects, such as those driven by radiation or convection, and require no additional energy to function. Notable examples of passive cooling are phase change materials (PCM).[11,12]

Spectral cooling approaches are interesting since they can work alongside other cooling technologies, given their unique nature. These solutions can also be divided into thermal radiative approaches and full spectrum management approaches, as presented in the review work by Zhao et al.[13] Thermal radiative approaches refer to the improvement of emissivity of solar cells and modules at wavelengths in the so-called atmospheric window wavelength band (8–13 μm) where heat from a photovoltaic device can be dissipated through dry clear air into outer space. The seminal work of Zhu et al.[14] numerically demonstrated the cooling potential of this mechanism for bare Silicon solar cells, with potential temperature reductions of 18.3 K. When this approach is applied to conventional photovoltaic modules, however, Zhao et al.[15] argued that its cooling potential was 1.75 K, mainly because conventional PV modules already present suitable emissivity in the range of interest due to the front glass. The authors argued that the approach is much more suitable to extraterrestrial applications, a similar conclusion reached by Safi and Munday,[16] who demonstrated, through the detailed balance method, that for space applications, the radiative cooling approaches could provide an absolute efficiency increase up to 2.60%, compared to a 0.87% when applied on a terrestrial application. Further studies by Zhao et al.[17] proved the radiative cooling potential of PV modules, particularly during nighttime (with temperature reductions up to 12°C), and the negative effect that environmental factors (increased relative humidity, wind speed, and ambient temperature) have on this potential. Further examples of radiative cooling approaches can be found in the abovementioned review by Zhao et al.[13] as well as in the works of Sato and Yamada[18] and Hu et al.[19]

Full-spectrum management approaches also consider the rejection of sub and above-bandgap radiation that contributes to temperature increases in photovoltaic modules. Khorrami et al.[20] created numerical models of spectral shields to assess the performance gains obtained by the rejection of 40% and 80% of the solar irradiation at wavelength values from the sub-bandgap range of 1 to 2.4 μm. The authors state that under high irradiance conditions (above 1,025 W/m^2), a shield with 80% reflectance provides a relative electrical efficiency improvement of up to 5.72%. Vaillon et al.[21] also showcased that sub-bandgap reflection and improved radiative cooling were interesting options for thermally managing PV modules. Sun et al.[22] performed an opto-electro-thermal simulation of the potential cooling provided to PV modules by the ideal rejection of sub-bandgap irradiance and enhancing emissivity in the atmospheric window range. The authors demonstrated temperature reductions as high as 10°C. Similarly, Heideier et al.[23] used numerical models and estimated a potential energy yield increase of 6.8% by ideally reflecting light at wavelengths above 1,000 nm for an equatorial location.

Other research efforts focus on feasible alternatives to achieve spectral management. Lu et al.,[24] for example, presented a technique that uses broadband textured imprinted glass that provides high emissivity within the atmospheric window combined with high transmittance within the visible spectrum, resulting in an increased short circuit current (5.12%) and power conversion (3.12%) compared to a standard case. Lin et al.[25] reported a relative increase in efficiency of 3.23% on a c-Si PV module by using flexible photonic architectures on polydimethylsiloxane. Cui et al.[26] studied the effect of thermal regulation coatings used either on the front side or back side of a glass/glass PV module. The authors found that an optimized TPX (polymethyl pentene) polymer matrix doped with SiO_2 particles located at the back side of the module provides radiative coating with temperature reductions of 1°C, which translates into an absolute increased efficiency of 0.21%. However, they also argue that, from an ideal standpoint, front-side spectral management has better cooling potential.

From this perspective, photonic crystals represent one of the most promising technologies. These devices affect the propagation of electromagnetic waves, allowing the tuning of the reflectance and transmittance of a surface via interference effects. This versatility makes them suitable for a variety of applications in solar cells and modules, like optional back reflectors,[27,28] coloring technology,[29–32] and light management in thin film solar cells.[33] Regarding thermal management, An et al.[34] studied the use of a combination of a one-dimensional (1D) photonic crystal based on 10 layers of nine different materials with a two-dimensional (2D) photonic crystal based on grated SiO_2. The combination provided high sub-bandgap reflection and high emissivity in the atmospheric window, providing a potential cooling on a c-Si solar cell of 10°C with an absolute increased power conversion efficiency of 0.43%. Akerboom et al.[35] studied a 2D photonic crystal based on Silica cylinders that provided a 3 K cooling potential to a c-Si module, representing a potential relative efficiency increase of 1.35%. Other examples of 2D photonic crystals can be found in the works of Zhao et al.,[36] which presented a combination of a 1D and 2D photonic crystal to enhance diurnal PV performance and nocturnal radiative cooling, and Perrakis et al.,[37] which simulated a 2D photonic crystal implemented on a PV module based on an interdigitated back-contacted (IBC) solar cell, which provided a cooling potential of 0.63°C and a relative efficiency increase of 3% thanks to a better optical behavior within the useful wavelength range (0.3–1.1 μm).

Perrakis et al.[38] compared the cooling performance effects on a commercial PV module of implementing a 2D photonic crystal (radiative cooling) versus the implementation of a 1D photonic crystal

(spectral management). Their results conclude that a 1D photonic crystal that rejects UV and sub-bandgap radiation while providing high transmittance in the useful range for c-Si solar cells outperforms the 2D device. One-dimensional photonic crystals are simpler to manufacture but present some technical challenges. Achieving high reflectance over a wide range of wavelengths demands the use of several different materials and a high number of layers. Additionally, they are required to have stable angular behavior, which can increase the complexity of the design. Fan et al.,[39] for example, designed a 1D photonic crystal based on ZnS and MgF_2 for a concentrated PV application in space. A total of 247 layers were required to meet the abovementioned requirements (reflectance at UV/IR, transmittance between 0.4 and 1.1 μm, and angular stability). Simulation results predicted a temperature reduction of 30°C and an absolute efficiency increase of 1.4%. Slauch et al.[40] designed and optimized several 1D photonic crystals with the purpose of cooling a PV module working under the climatic conditions of Golden, Colorado. The authors demonstrated that achieving angular stability and good optical performance required designs with 34 layers and four materials for a photonic mirror located in the air/glass interface and 35 layers and two materials for one placed between the front glass and the EVA. Simulation results predicted an increase in energy output of up to 3.4% for the selected location.

Li et al.[41] also introduced a comprehensive study on the thermal management of solar cells using a 1D photonic crystal that rejects light at wavelengths that only contribute to the temperature increase of an encapsulated cell without any contribution to its electrical output. The device presents near-ideal performance and consists of alternating layers of four materials (TiO_2, Al_2O_3, SiN, and SiO_2) with a total count of 45 layers. The proposed filter provides a solar cell temperature reduction of 5.7 K compared to a standard, uncoated encapsulated solar cell under the same illumination conditions.

High layer counts imply complexity in manufacturing, and simplified designs could contribute to widespread implementation. This work explores the experimental implementation of simple 1D photonic crystals (henceforth referred to as optical filters) to be used as PV thermal managing devices and the related modeling to simulate the energy yield and the degradation rate of PV modules endowed with such filters. This work shows that it is possible to produce a reflectance profile containing two high reflectance peaks with a low layer count by following basic optical filter design rules. These reflectance peaks are tailored to partially reflect unwanted infrared (IR) irradiation and light at wavelength values where a c-Si solar cell presents high thermalization losses. Reducing thermalization also entails reducing electrical output, which produces designs with a reduced performance compared to more sophisticated alternatives such as those presented before. Such comprehensive designs are preferred, provided adequate economic feasibility of their implementation.

The main contribution of this study is the implementation of a full simulation framework that considers not only the impacts of temperature on the instantaneous performance of a PV module but also its expected lifetime, thus allowing the analysis of when these simplified optical filters can provide a net positive benefit when implemented on PV systems.

This article is organized as follows. Section 2 presents an overview of the modeling framework. Section 3 presents the steps to design a simplified optical filter for thermal management. Section 4 presents the results from simulation work on how the filter affects the overall performance in various locations. Additionally, it studies the potential benefits of implementing the thermal filter concerning an improved degradation rate. Section 5 draws the main conclusions. At the end of this document, the reader can find all the experimental work and model validations.

2 | MODELING FRAMEWORK

The computational model framework follows the same approach presented in our previous work.[42] The models consist of spectrally resolved algorithms that estimate the effective irradiance reaching the solar cell, its operating temperature, and its electrical energy output at any instant. The Simple Model of the Atmospheric Radiative Transfer of Sunshine (SMARTS)[43] allows the estimation of the solar spectrum. These spectra are used for optical, thermal, and electrical assessments.

The optical pillar utilizes two software packages: GenPro4[44] and OptiLayer®.[45] The former produces four main outputs: first, it matches the spectral behavior of the chosen solar cell optically. The SunPower Maxeon® II interdigitated back-contacted (IBC) solar cell[46] is the selected structure in this work. Second, it computes the optical current densities J_{opt} (in mA/cm^2) of each layer within a PV module, which are the basis of the irradiance scaling factors τ_0 and i_{opt}, defined mathematically as

$$\tau_0 = \frac{J_{opt(cSi)}}{\sum J_{opt(Lay)} + J_{opt(cSi)}}, \quad (1)$$

$$i_{opt(\theta)} = \frac{J_{opt(\theta)}}{J_{opt(0^\circ)}}. \quad (2)$$

In Equation (1), $J_{opt(cSi)}$ (mA/cm^2) represents the optical current density of the c-Si solar cell. $J_{opt(Lay)}$ (mA/cm^2) is the optical current density of each layer within a PV module that contributes to losses (reflectance or absorptance), such as glass, encapsulant, anti-reflective coating, emitter, and the optical filter. τ_0 is a factor that accounts for the optical losses at normal incidence. Equation (2) defines the factor that accounts for the optical loss at different angles of incidence (AOI). It is calculated by dividing the optical current density at any given AOI $J_{opt(\theta)}$ by the optical current density at normal incidence $J_{opt(0^\circ)}$. Notice that, at normal incidence, $J_{opt(0^\circ)} = J_{opt(cSi)}$. The effective irradiance reaching the solar cell G_{cell} depends on these two factors as they scale the plane of array irradiance G_{POA} as follows:

$$G_{cell}(\theta) = \tau_0 \cdot i_{opt}(\theta) \cdot G_{POA}. \quad (3)$$

Third, GenPro4 helps in the first stage of the design, which aims to find an adequate range of wavelengths at which thermal management produces as low optical loss as possible at normal incidence.

OptiLayer® allows finding potential design candidates that ensure low optical losses at different angles of incidence via second-order optimization methods.

Lastly, GenPro4 provides the spectral absorptance of all the layers within a PV module, which are fed into the thermal model. This model uses a two-dimensional finite volume transient approach that estimates the volumetric heat produced within every layer as a function of wavelength. The model provides the solar cell operating temperature (T_{cell}) as output, which serves as a guideline for the design of the thermal filter.

T_{cell} and G_{cell} are the inputs for a two-diode equivalent circuit electrical model. After an iterative process (given the direct relationship between electrical power and thermal power in the cell), the maximum electrical output power at each instant is obtained.

3 | THERMAL FILTER DESIGN AND OPTIMIZATION

Optical filters reflect light by depositing thin layers of dielectric materials with a mismatch in their refractive indexes n. As mentioned above, the selected optical filter structure in this study consists of two materials, one with a high refractive index (n_H) and another with a low refractive index (n_L). These materials are deposited sequentially in pairs, and, depending on the wavelength value (λ_0, in nm) at which high reflectance is desired, the thickness of the layers (d, in nm) is calculated via the quarter wavelength optical thickness (QWOT) formula.[47]

$$d_{L|H} = \frac{\lambda_0}{4 \cdot n_{L|H}} \tag{4}$$

In literature, it is common practice to notate a QWOT layer as the capital letter of its refractive index hierarchy. Thus, H refers to a layer with refractive index n_H and thickness d_H (nm) given by Equation (4), and L is the corresponding value for a layer with a lower refractive index. This work follows this same notation scheme. When a layer does not have a thickness value equal to that given by Equation (4), the presented notation is a fraction of it. For example, 0.5H represents a layer of the high refractive index material with a thickness that is half of that of the QWOT value.

When stacks of several pairs of layers are involved in the design, the notation utilized here follows the form $(LH)^p$, where p is the number of pairs of LH layers. More detailed information about the presented designs is available in Appendix B. The selected materials are silicon nitride (SiN_X), represented henceforth as H, and silicon dioxide (SiO_2), represented as L. These materials were selected due to their optimal optical properties and ease of manufacturing, as explained in Ortiz Lizcano et al.[42] The appendix at the end of this document provides details on the optical properties of these materials.

The design of the thermal filter starts by studying the optical behavior of the selected IBC solar cell structure. Figure 1a presents the measured data. It is noticeable that the cell either transmits or rejects a significant portion of the near-infrared (IR) spectrum (from 1,200 to 1,800 nm). This IR behavior is due to the architecture of the IBC solar cell itself, and different topologies will show different behaviors in this region.[48] Optical simulations of a PV module help analyze its spectral absorbed irradiance (see Figure 1b). It is noticeable that most of the spectrum in the abovementioned near-infrared region range is not absorbed.

3.1 | Infrared rejection

Previous studies have shown that high rejection of the near-infrared region could have potential cooling benefits on PV modules.[48] Rejection of light on this wavelength range eliminates thermal gain without producing an optical loss. Therefore, it is interesting to see the potential cooling effect on the selected solar cell. The optical filter must provide high reflection for a wavelength range from 1,200 to 1,800 nm and high transmittance from 300 to 1,200 nm. Fulfillment of these requirements usually results in very complicated structures.

Figure 2a presents an example of such a complex filter. The initial design of the filter consisted of layers arranged as $0.5A|(AB)^{20}|B|0.5A$, based on the work by Seoane da Silva,[49] where A and B refer to QWOT layers of MgF_2 and TiO_2, respectively. OptiLayer® allowed optimization of this starting design by using the needle technique.[45,50,51] The resulting design consists of 81 layers, whose simulated reflectance at normal incidence is presented in Figure 2b. After the optimization, the final thickness values of the materials differ from their starting QWOT value, and Figure 2a only depicts their order. The complete details about this design can be found in Table B1.

The complete optical model of a PV module with this IR filter implemented (see Figure 2a) aimed to study the predicted effect on the operational cell temperature. The module was considered to operate at maximum power point under NOCT conditions. The optical, physical, and thermal properties are presented in Appendix A. The results were then compared to the case of the same PV module without the filter implemented. The steady-state temperature on the solar cell obtained for the standard PV modules was estimated at 45.2°C. Figure 3a shows the temperature profile of the entire module for this case. A PV module with the optic filter implemented presents a steady state temperature of 41.7°C, representing a reduction of 3.5°C. The profile for this case is shown in Figure 3b.

Implementing such a complex filter design for this cell architecture does not provide a significant temperature reduction. Moreover, optical filters have markedly different behavior at different angles of incidence (AOI) (see Figure 2b). Estimating the scaling factors τ_0 and i_{opt}, defined by Equations (1) and (2), allows analysis of the optical losses produced by the filter. The absolute optical loss produced by the infrared filter at normal incidence is 1%, as presented in Table 1.

The angular optical loss is significantly higher for the case of the PV module with an IR optical filter compared to the standard, as presented in Figure 4. The filter will substantially reduce the effective irradiance reaching the solar cell for values of AOI above 20°. At 50°, for example, the scaling factor i_{opt} of a standard PV module has a

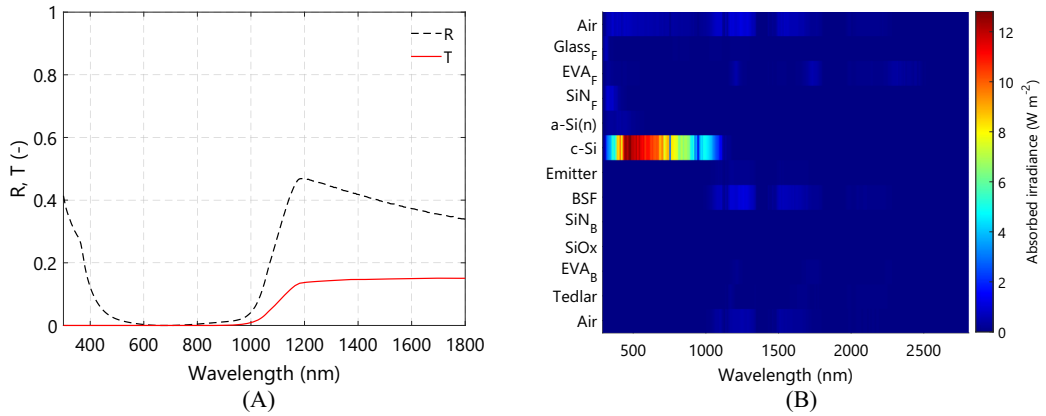

FIGURE 1 (a) Measured reflectance (R) and transmittance (T) for a SunPower Maxeon II IBC solar cell (non-encapsulated) using a PerkinElmer Lambda Spectrophotometer. (b) Heatmap of the simulated absorbed irradiance of a PV module endowed with an IBC solar cell. The heatmap showcases that most of the irradiance on the near-infrared does not affect the PV module. The subscripts F and B refer to the front and back layers of the module with respect to the c-Si cell.

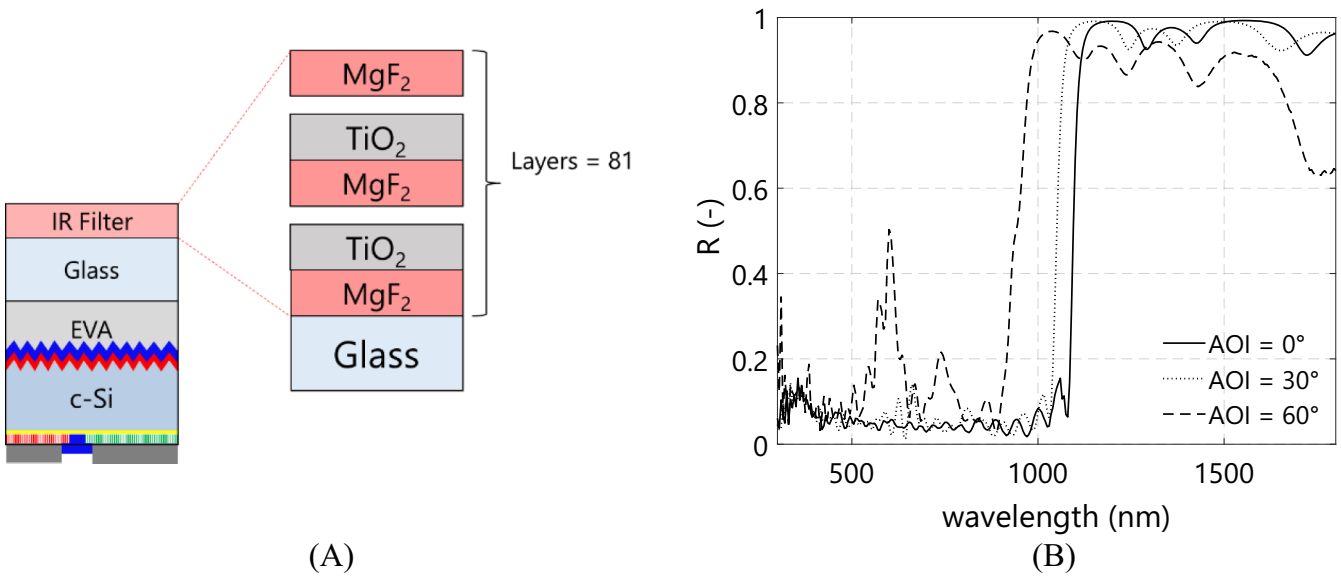

FIGURE 2 (a) Final design layout of a near-ideal optical filter with high reflection in the near-infrared region and high transmittance from 300 to 1,200 nm. (b) Simulated reflectance profile of the complete optical model of the PV module, with the optimized IR optical filter deposited on the front surface of the glass, for three different angles of incidence (AOI). At higher values of AOI, the reflectance of the filter shifts towards lower wavelength values. Moreover, additional reflectance peaks appear between 500 and 700 nm, increasing the optical loss.

value of 0.94. Implementing the IR filter will reduce the value of such a factor to 0.8, an additional 15% loss. Improving the angular behavior of the filter will only increase its complexity. With its high layer count and limited thermal benefits, this design has no practical application for a PV module made with IBC solar cells.

3.2 | Reduction of thermalization losses

Another option to provide thermal management on the solar cell is by reducing its thermalization losses. Thermalization is one of the primary sources of heat within a solar cell. Simulations of the PV module under NOCT conditions help highlight the range of wavelengths at which the difference between absorbed irradiance and extracted power is the largest. The selected optical model for the PV module, in this case, differs from that of Figure 2a. To ensure protection from environmental damage, the filter is positioned at the backside of the front glass, as shown in Figure 5. Figure 6a highlights this difference. The selected wavelength of interest was from 400 to 500 nm. Although the difference between absorbed and extracted power is the highest at 470 nm, lower wavelength values allow thermal management with lower optical losses.

Equation (4) allows finding the thickness values of the H and L layers for $\lambda_0 = 450$ nm. The higher the number of pairs p, the higher

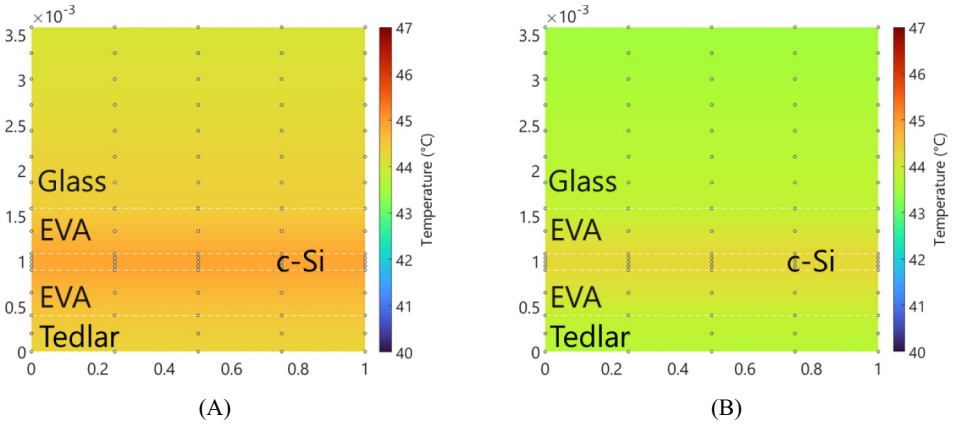

FIGURE 3 Thermal profile as a function of a PV module's width (*x* axis, in meters) and depth (*y* axis, also in meters) depicting (a) the steady-state temperature profile of a PV module under NOCT conditions, with a cell temperature value of 45.2°C. (b) The steady-state temperature profile of a PV module with the optical filter is presented in Figure 2a. The filter reduces the cell's operating temperature by 3.5°C to a value of 41.7°C.

TABLE 1 Simulated value of τ_0 for both PV module layouts

Parameter	Standard	IR filter
τ_0	0.93	0.92

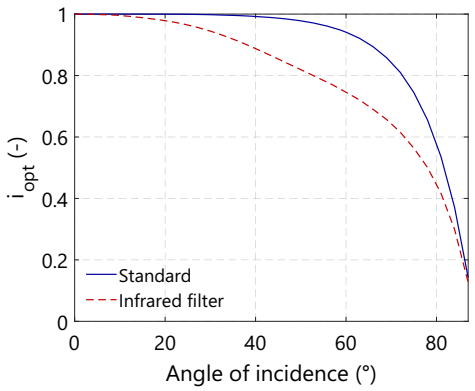

FIGURE 4 Simulated value of i_{opt} as a function of the angle of incidence for a standard and an IR filter PV module

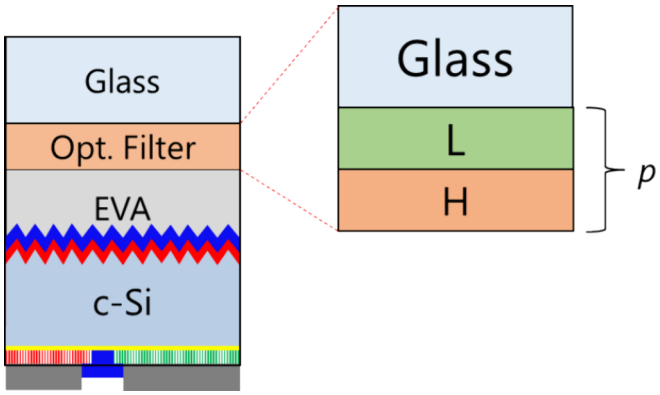

FIGURE 5 Optical model of a PV module with an optical filter deposited on the backside of the front glass. The filter is made of *p* pairs of LH layers and is the basis for the optimization presented in this section. In the experimental work, the filter was deposited into a glass substrate via plasma-enhanced chemical vapor deposition (PECVD). Afterward, the glass was used as the front layer of an encapsulated solar cell, creating a mini-module. The mini-module was manufactured using a vacuum laminator with a curating temperature of 140°C. In the optical model, no air layer is considered at any interface within the mini-module.

the filter's reflectance at λ_0. However, as established by Macleod,[61] a high layer count produces an equal amount of reflectance ripples around the central reflectance peak. These ripples, alongside the wider reflection range, translate into significant optical losses. Furthermore, at higher angles of incidence, the reflection peak shifts towards lower wavelength values, meaning that the angular stability of the optical filter must be guaranteed to maintain the cooling potential. This work suggests and implements the use of a more straightforward design strategy, that is, using a harmonic peak produced by a filter with a high value of λ_0. These peaks appear at $\lambda_0/3$, $\lambda_0/5$, $\lambda_0/7$, and lower harmonics for the case of filters with an $(LH)^p$ layout. Their maximum reflectance value decreases as the harmonic order increases, meaning that the harmonic with the highest reflectance peak will be at $\lambda_0/3$.

Figure 6b presents the reflectance profile of three different filters that guarantee a peak at the wavelength range of interest for different values of λ_0. The practical advantage of the design with a value of $\lambda_0 = 1{,}350$ nm resides in three main aspects. First, the filter produces a reflectance width of around 60 nm, less than the other options, which in both cases surpasses 100 nm, thus reducing optical losses. Second, the ripples around the 450 nm reflectance peak are significantly lower than their counterparts, improving optical performance. Lastly, the central reflectance peak at 1,350 nm has an additional cooling contribution that its alternatives lack.

Narrow reflectance peaks across the wavelength range of interest (400–500 nm) can be achieved simply by shifting the value of λ_0 from 1,200 to 1,600 nm. The number of pairs *p* that achieved near unity reflectance is 11, as presented in Figure 7a. Notice that, for the sake of clarity, the units of λ_0 are expressed in μm on the graphs.

Models of the different filter candidates were obtained by changing λ_0 from 1,200 to 1,600. The right axis of Figure 7b shows the calculated difference (ΔJ_{opt}) between the optical current density of a module without an optic filter and the possible candidates at STC. On this axis, the greater the value of ΔJ_{opt}, the greater the optical loss.

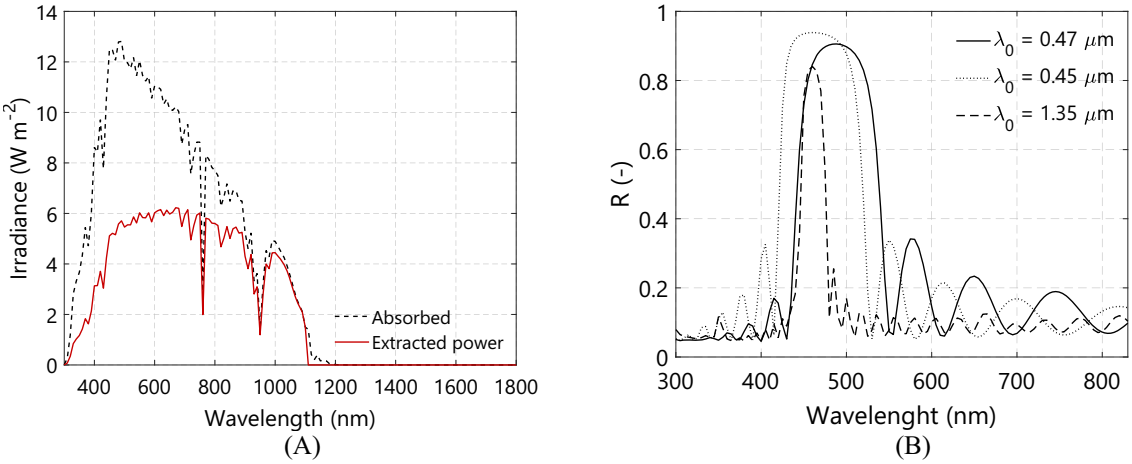

FIGURE 6 (a) Absorbed and extracted power of a PV module based on IBC solar cells by simulating the behavior of the PV module at maximum power point under NOCT conditions. (b) Reflectance profile of three different optic filter designs that provide high reflectance at the wavelength range of interest (400–500 nm, focused towards 470 nm) based on their value of λ_0

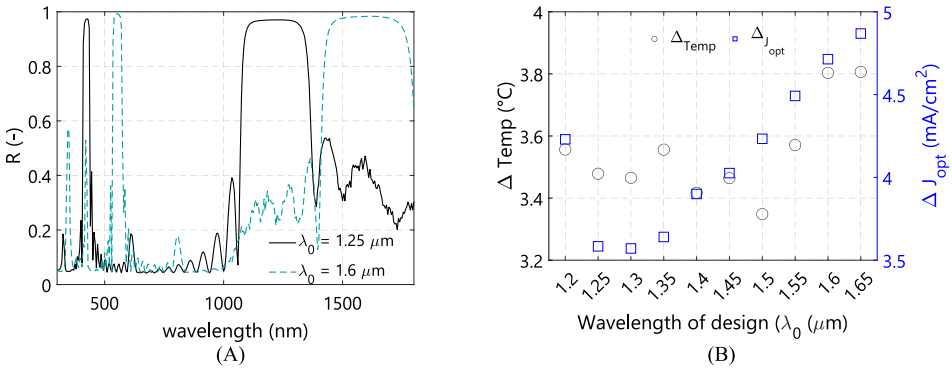

FIGURE 7 (a) Reflectance profile of the two limits of λ_0 studied (1,200 and 1,600 nm) that produces narrow reflectance peaks ranging from 400 to 533 nm. (b) Solar cell temperature difference ($\Delta Temp$ in °C) and optical current density difference (ΔJ_{opt} in mA/cm^2) between an encapsulated solar cell with and without a deposited thermal filter. The greater the value of temperature difference, the better the cooling provided by the filter. On the contrary, higher values of current density difference represent higher optical losses, leading to reduced electrical output.

Notice that a filter with $\lambda_0 = 1{,}200$ nm presents a more significant loss than one with λ_0 up to 1,450 nm. This higher loss is because part of the high reflectance width around 1,200 nm falls at wavelengths at which a c-Si still produces current, such as 900 nm. Once λ_0 increases, this reflectance range shifts more and more towards the IR region, where it does not produce any optical loss.

Examination of the steady state solar cell temperature at NOCT conditions also provides insights into the optimal value of λ_0. The temperature difference (ΔT_{cell}) compared to a PV module without the filter is presented on the left axis of Figure 7b. This parameter represents the potential cooling power, so the greater the value of ΔT_{cell}, the better the filter's performance. A filter should have relatively good cooling performance and low optical loss. The left axis in Figure 7b shows that the behavior of ΔT_{cell} differs from that of ΔJ_{opt}. From the starting value of $\lambda_0 = 1{,}200$ nm, the temperature difference lowers slightly until $\lambda_0 = 1{,}300$ nm. The differences are marginal and driven mainly by the shift of the high reflectance band and its ripples at around 900 nm towards higher values.

At $\lambda_0 = 1{,}350$ nm, the harmonic reflectance peak coincides with the peak differences between absorbed and extracted power. Once that peak shifts towards higher wavelength values, the temperature difference drops again for $1{,}400 < \lambda_0 < 1{,}500$ nm. The temperature difference then increases until $\lambda_0 = 1{,}600$ nm, caused by harmonics at λ_0 /5 and λ_0/7 that contribute to the cooling effect and produce higher optical losses (see the dashed reflectance profile in Figure 7a). A suitable value of λ_0 lies between 1,300 and 1,350 nm. At normal incidence, a filter with a λ_0 value of 1,300 nm produces lower optical current losses, albeit with a slight reduction in cooling potential compared to one with $\lambda_0 = 1{,}350$ nm. However, at higher angles of incidence, the shift of the reflectance peaks towards lower wavelength values on the filter with $\lambda_0 = 1{,}300$ nm presents higher optical losses than the one with $\lambda_0 = 1{,}350$ nm, as depicted in Figure 8a. The relative optical loss, calculated via Equation (2) for both filters, indicates that at values of AOI greater than 20°, the filter with

$\lambda_0 = 1{,}300$ nm presents higher optical losses, reaching a maximum of 4% around AOI $= 60°$, compared to the filter with $\lambda_0 = 1{,}350$ nm (see Figure 8b). This relative optical loss was estimated using the following equation:

$$Relative\ loss(\%) = -\frac{i_{opt\,\lambda=1300} - i_{opt\,\lambda=1350}}{i_{opt\,\lambda=1350}} \cdot 100, \quad (5)$$

where $i_{opt\,\lambda}$ is the angular optical loss factor as defined by Equation (2).

Since simplicity is at the core of this work, a filter with $\lambda_0 = 1{,}350$ nm was considered the best in providing a sensible thermal and optical performance combination.

Optical losses are reduced by lowering the value of p. As with λ_0, the optimization involves a tradeoff between optical loss and cooling improvement. Figure 9a shows how reducing the value of p impacts both the optical current density J_{opt}, estimated at STC, and the steady-state solar cell temperature T_{cell}, estimated at NOCT. This difference in scenario (STC vs. NOCT) was selected to optimize the optical effect produced by the different filter layouts separately, for the same value T_{cell}, and later study its effect on the steady-state temperature reached by the cell under the environmental conditions of the NOCT scenario. Finding a practical value of p was done by comparing the different values of p with those designs that provide the best performance in terms of J_{opt} ($p = 2$) and T_{cell} ($p = 11$). Figure 9b presents the trends obtained. Reducing the number of pairs to $p = 4$ causes a gain in the optical current density J_{opt} of 0.82 mA/cm^2 while increasing the value of T_{cell} by 0.55°C, compared with the abovementioned best-performing designs.

Reducing the number of pairs decreases the optical loss depicted by τ_0. An additional strategy for reducing the optical loss consists of eliminating the ripples produced between the two main reflectance peaks. These ripples appear both at lower and higher wavelengths

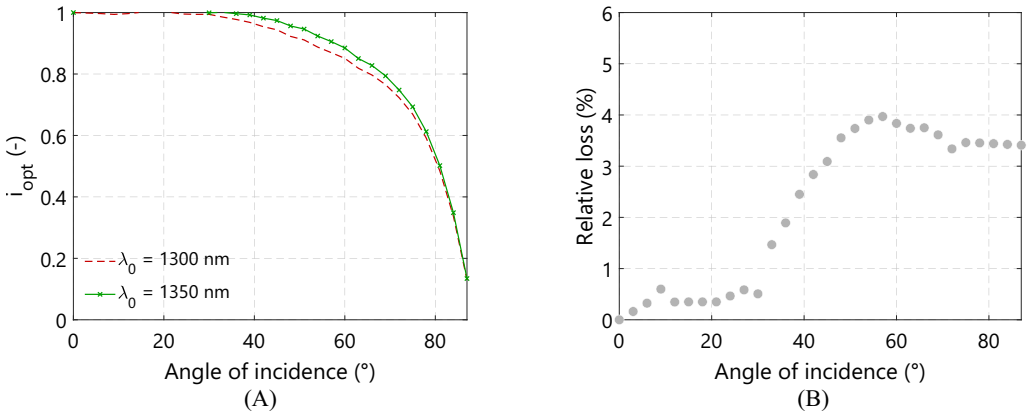

FIGURE 8 (a) Simulated angular factor i_{opt} for a thermal filter with $\lambda_0 = 1{,}300$ nm (dashed line) and $\lambda_0 = 1{,}350$ nm (line with cross markers). The trend of the filter with $\lambda_0 = 1{,}350$ nm indicates a better optical performance. (b) Relative loss produced by a filter with $\lambda_0 = 1{,}300$ nm compared to one with $\lambda_0 = 1{,}350$ nm for different angles of incidence. Notice that the negative sign in Equation (5) transforms the calculated relative loss into a positive number for easier understanding.

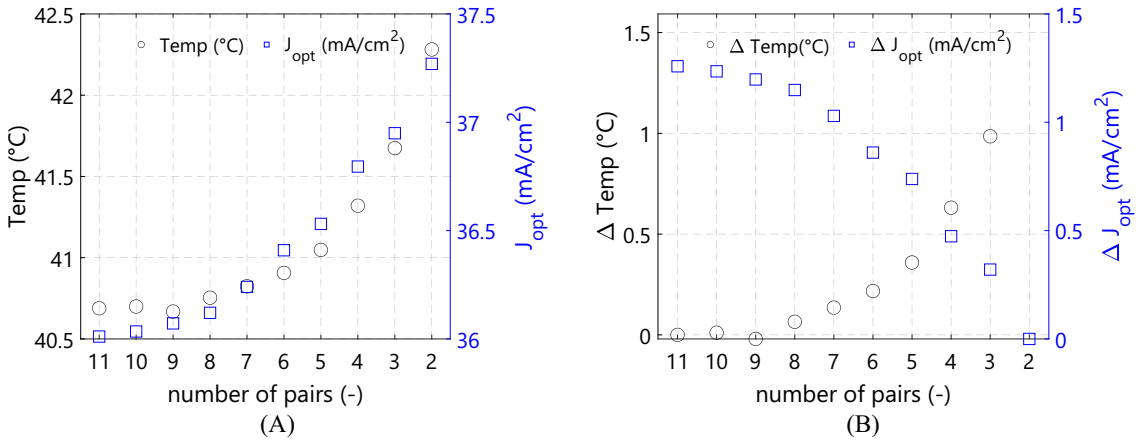

FIGURE 9 (a) (Right) Simulated optical current density in mA/cm^2 (under STC conditions) and (left) steady state temperature in °C (under NOCT conditions) as a function of the number of pairs for an optical filter with an $\lambda_0 = 1{,}350$ nm. (b) (Right) Differences in optical current density (mA/cm^2) with respect to the filter with the highest current density ($p = 2$). (Left) Differences in steady-state temperature with respect to the filter that provides the lowest cell operating temperature ($p = 11$)

from the central reflectance peak (determined by λ_0). They can be suppressed by placing layers with half QWOT at both ends of the filter. If the layer belongs to material H, the ripples for wavelengths greater than λ_0 are suppressed. Conversely, placing material L at each end eliminates ripples below λ_0. This latter option is applied in this case. Figure 10a shows how going from an $(LH)^4$ design towards a $0.5L|(HL)^3|H|0.5L$ design significantly eliminates ripple without major effects on the reflectance peak at 450 nm.

As presented in the case of the IR filter, i_{opt} also represents an essential optical loss that needs optimization. The angular behavior of the simplified filter based on $0.5L|(HL)^3|H|0.5L$ still presents important losses. Figure 10b shows the behavior of this filter at two different angles of incidence, 0° and 50°. At 50°, the high reflectance peak shifts to lower wavelength values. For example, at 1,000 nm, the filter presents a reflectance value of 0.4, which translates into substantial optical losses on the PV module. Notice that the results presented in Figure 10 belong to an optical system of air|glass|filter|air. This simplified optical system is easier to optimize in OptiLayer®.

OptiLayer® was used to improve the angular stability of the filter by using its second-order optimization algorithm, the so-called *needle technique*.[45,50,51] The main inputs for the deployment of the needle technique are the initial filter design, the desired final reflectance, and, for each wavelength value of reflectance, the accepted tolerance in percentage. The selection of the target reflectance and the allowed tolerance per wavelength plays an important role in the complexity of the filter's design. Figure 11a gives an example of a potential reflectance target. The target aims to eliminate the remaining ripples to reduce optical losses further while keeping both areas with high reflectance. The blue and green areas depict the upper and lower tolerance limits. These target and tolerance values allow the algorithm to accept any value of reflectance that falls within the colored areas. However, with this target, the algorithm also forces the elimination of the small ripples. Reduction of these ripples will have a less significant impact on the incurred optical losses compared to the improvement of angular stability. Figure 11b presents a more appropriate reflectance target. The ripples are considered acceptable, and the effort in the optimization procedure focuses on a slight reduction of the reflectance at 450 nm (notice the difference between the blue and green areas, which forces the algorithm to reduce the peak) and to maintain angular stability. The target is fed

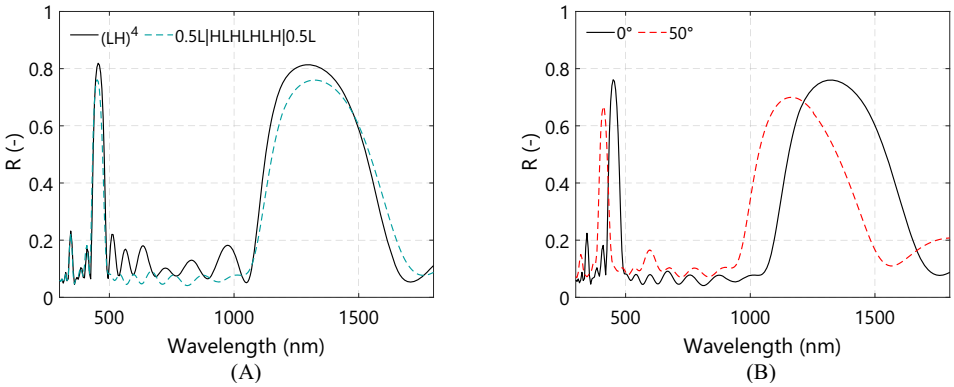

FIGURE 10 (a) Reduction of ripples by changing the layout of the filter from $(LH)^4$ to $0.5L|(HL)^3|H|0.5L$. (b) Even though the ripple is substantially reduced, the angular behavior still presents shifts that produce significant optical losses on the PV module.

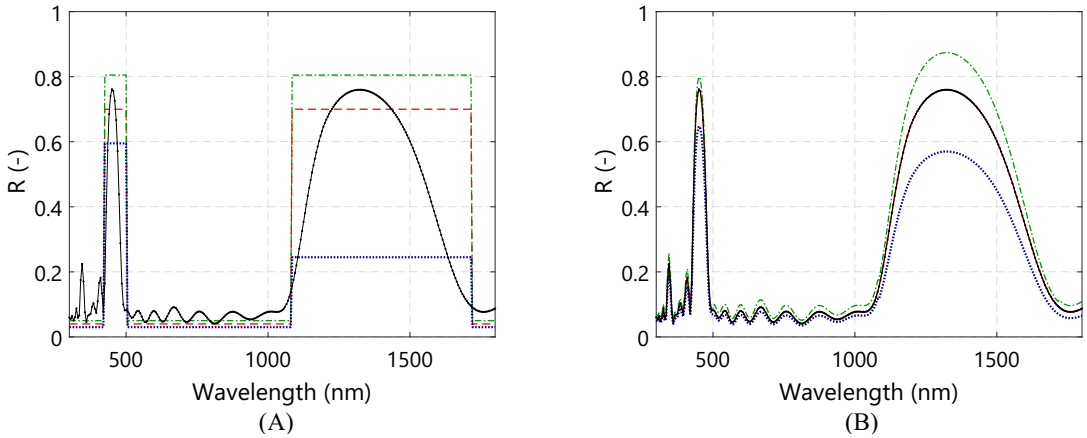

FIGURE 11 (a) Original reflectance (continuous dotted line), target reflectance (red dashed line), and tolerance ranges (delimited by the dash-dotted green and dotted blue lines) for a highly optimized filter design. Such strict target leads to highly complex and thick filter designs. (b) A more practical approach is to use a target reflectance that mimics the reflectance behavior of the initial design and set tolerance limits to the algorithm that also follows the reflectance pattern. Acceptable losses from small ripples force the algorithm to focus mainly on reducing the peak at 450 nm and improving angular stability, keeping the design of the optical filter practical.

into OptiLayer® as being the same for normal incidence, 20° and 50°.

OptiLayer® has different options for automating the optimization process. An explanation of the different approaches can be found in the developer's work.[45] However, the automation process is extremely fast, inserting new layers quickly. Filters obtained by this approach quickly reach a layer count that easily surpasses 20 layers. The aim of this work is to obtain filters that have a relatively low layer count. To achieve this, the layer insertion was done manually according to the value of a merit function.[52] The merit function estimates, according to the position where a new layer is added, if the resulting reflectance gets closer (negative value) or further (positive value) from the target.

The resulting filter (hence referred to as a Thermal filter) consists of 15 layers with no repetitive thickness values, and its detailed design is presented in Table B2. The main objective of the optimization was to improve angular behavior while limiting the number of layers to a practical value. Easy manufacturing was deemed preferable compared to near-ideal optical behavior. For comparison, Figure 12b presents the reflectance profile of this thermal filter at the same angle of incidence values as its base design once implemented on a PV module. Notice that at 1,000 nm, the thermal filter has a reflectance value of 0.23, which reduces optical losses (comparing Figure 12a,b). The trend depicted by the i_{opt} scaling factor of this thermal filter showcases the

TABLE 2 Simulated values of τ_0, estimated under STC conditions, and T_{cell}, estimated under NOCT conditions for the baseline filter design (0.5L|(HL)^3|H|0.5L) and the final thermal filter design after optimization (15 non-QWOT layers) via needle technique

Filter 0.5L|(HL)^3|H|0.5L		Thermal filter	
τ_0 (–)	T_{cell} (°C)	τ_0 (–)	T_{cell} (°C)
0.80	41.32	0.85	41.86

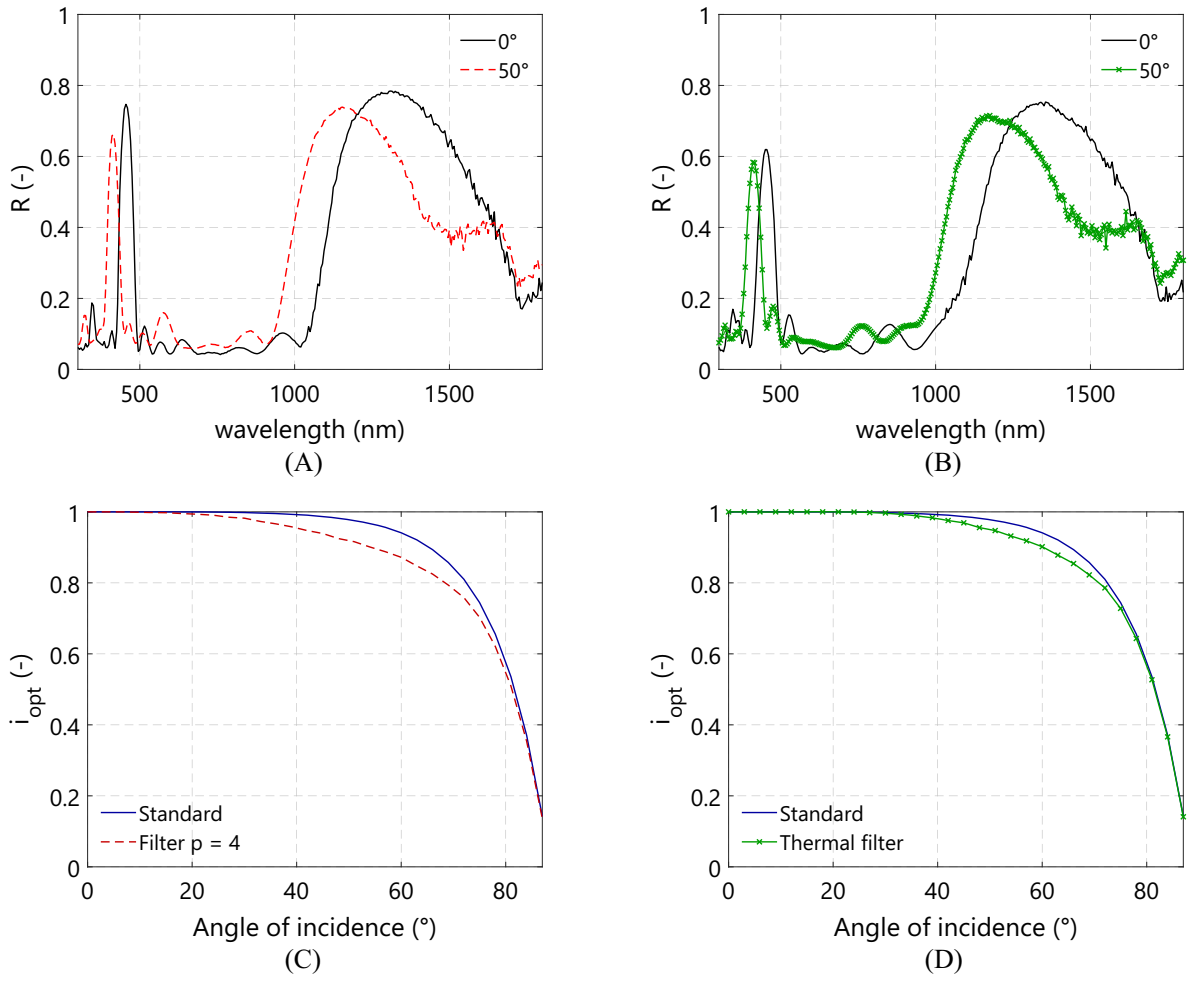

FIGURE 12 (a) Simulated reflectance at normal incidence and an angle of incidence equal to 50° for a filter with a 0.5L|(HL)^3|H|0.5L layout implemented on a full PV module. (b) Simulated reflectance of the improved thermal filter under the same angle of incidence conditions. Notice the reduced value of (R) at 1,000 nm for the case of AOI = 50°. The optimization technique shifted the high reflectance zone towards higher wavelengths while keeping the peak at the desired value of 450 nm. (c) The simulated trend of the angular scaling factor i_{opt} for the filter with $p = 4$ compared to a standard module without the filter. (d) The same trend simulated for the thermal filter highlights the results from the optimization process, reducing the gap with respect to the standard module.

improvement with respect to the filter with 0.5L|(HL)^3|H|0.5L. Moreover, the peak at 450 nm was reduced to improve the value of τ_0.

The optimization procedure increased the value of τ_0 from 0.80 to 0.85. An increased solar cell temperature follows this reduction of the optical loss at normal incidence. Simulations at NOCT predict that this increase amounts to 0.54°C compared to the baseline design (0.5L|(HL)^3|H|0.5L). The overall results from the simulations are presented in Table 2.

More details of the designed thermal filter are explained in the appendix.

4 | EFFECT ON PV PERFORMANCE AND DEGRADATION RATE

A study of the overall effect of adding a thermal filter to a PV module was done by simulating the DC energy yield obtained from two modules, one with the thermal filter and one being a standard module. The chosen locations for the study were Delft (in the Netherlands) and the city-state of Singapore. The weather data were extracted from the PVGIS database[53] for five consecutive years (2015–2020). The PV modules were set to their optimal tilt and azimuth for each location. The measured data obtained from the SunPower IBC solar cell were used to model the PV modules. The resulting current (I) versus voltage (V) curve was obtained experimentally and is presented in Figure 13. Each module is considered to have 96 solar cells connected in series. Even though the IBC solar cells under test are bifacial, we consider that the transmitted light through them is lost. Therefore, current losses and the effect of the back sheet were not considered for the simulations. The total DC power was obtained by estimating the individual contribution of each cell, all operating under the same conditions. The data for the module under STC conditions are presented in Table 3. The temperature coefficients were taken from the data sheet published by SunPower for their Maxeon® Gen II solar cell.

Simulations had a time resolution of hours. Estimation of hourly DC yield and operating cell temperature for each module were used to analyze the overall effect of implementing the thermal filter. Results show that thermal gain cannot compensate for the optical loss. In Delft, a PV module with a thermal filter presents a relative DC energy yield loss compared to a standard module of 10.01%. The 98th percentile value from the instantaneous temperature difference between the standard module and the module with the thermal filter was estimated at 2.20°C. The estimated relative energy loss in Singapore was 9.76%, with a 98th temperature difference of 2.45°C. The module with the thermal filter presented maximum and mean values of T_{cell} lower than those obtained for the standard module. Table 4 presents the main results from the simulation work for both locations and modules. No degradation mechanism was accounted for at this first stage of simulations.

To evaluate the yearly degradation rates/lifetime of the modules, a physics-based approach that considers various aspects that might influence PV reliability[54] was used. In this approach, the electrical model is modeled as time and climate/stress factors (i.e., module temperature, relative humidity, and UV dose) using the degradation rate and reliability models.[4] The outputs of the degradation model are the time series of electrical parameters (power, short circuit current, open circuit voltage) with degradation. The 5 years of weather data were replicated to estimate both locations' annual degradation rates (DR). The UV component was estimated to be a 5% fraction of the plane of array irradiance components obtained from the weather data.

The calculated normalized performance ratio (PR) serves as the key performance indicator to determine the useful lifetime of a module. The limiting value is a normalized PR of 0.8. The time it takes a module to reach this limit is considered its useful lifetime (LT), expressed in years. The lifetime energy yield was defined as the total energy produced by the module until it reached the normalized PR limit.

In the case of Singapore, the thermal filter increases the lifetime of the PV module by 2 years. A standard PV module reaches its limit in 22years (DR = 0.98%/year), whereas the module with the thermal filter does it in 24 years (DR = 0.89%/year), as shown in Figure 14a. During its lifetime, the standard PV module produces 8,934.09 kWh. The PV module with the thermal filter produces 9,212.85 kWh, representing a relative energy yield gain of 3.12%. This gain means that the

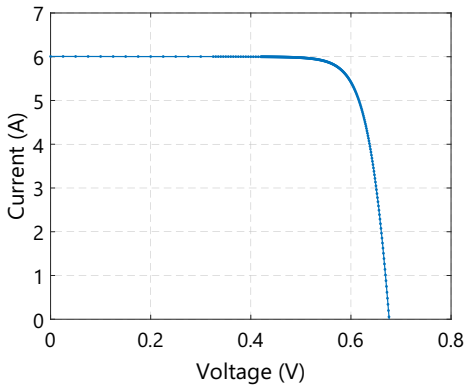

FIGURE 13 IV curve of a single encapsulated SunPower IBC solar cell utilized for the simulation work

TABLE 3 PV module parameters

Parameter	Value
I_{SC} (A)	6.005
V_{OC} (V)	64.93
I_{MPP} (A)	5.71
V_{MPP} (V)	55.66
P_{max} (W)	317.82
$\delta V_{OC}/\delta T$ (mV/°C)	−1.84
$\delta I_{SC}/\delta T$ (mA/°C)	2.60
$\delta P_{max}/\delta T$ (%)	−0.35

Note: The values belong to a module containing 96 solar cells without the thermal filter installed.

TABLE 4 Simulation results of the 5-year DC energy yield for two 96 IBC solar cell PV modules

	Standard PV module			PV module + thermal filter			
	DC yield (kWh)	T_{cell} avg (°C)	T_{cell} max (°C)	DC yield (kWh)	T_{cell} avg (°C)	T_{cell} max (°C)	ΔT_{p98} (°C)
Delft, NL	1,876.30	18.73	43.22	1,688.40	17.91	41.02	2.20
Singapore	2,749.80	36.11	51.83	2,481.40	35.02	49.38	2.45

Note: One standard PV module and another with a thermal filter implemented beneath the front glass. Hourly simulations were run for five consecutive years using weather data from the PVGIS database.

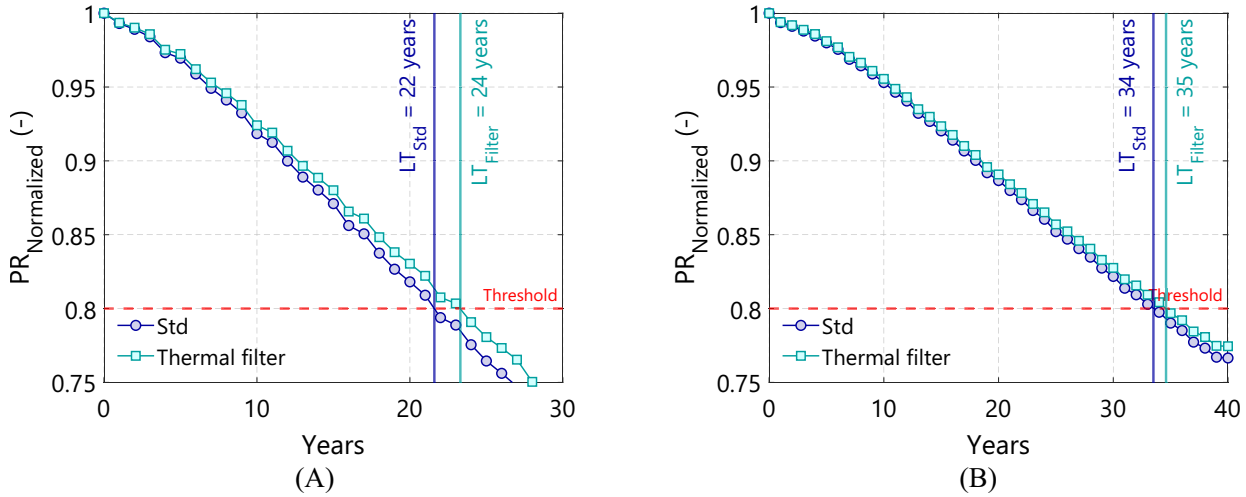

FIGURE 14 (a) Renormalized performance ratio (PR) of a standard PV module and a PV module with a thermal filter installed in Singapore. (b) The renormalized PR of both modules is located in Delft.

TABLE 5 Simulated degradation rate results for a standard PV module and a PV module with a thermal filter

	Singapore		Delft	
	Standard	PV + T. filter	Standard	PV + T. filter
RH (%)	84.45	84.45	83.11	83.11
UV dose (kWh/a/m^2)	79.74	79.74	52.56	52.56
DR (%)	0.98	0.89	0.57	0.55
Lifetime (years)	22.00	24.00	34.00	35.00
DC lifetime (kWh)	8,934.09	9,212.85	9,153.57	8,925.29

Note: Values of ultraviolet light and relative humidity (RH) were extracted from the weather data. For the case of UV light, the values were estimated as a 5% fraction of the irradiance components.

net effect of the thermal filter on the DC energy production of a PV module, despite the initial optical loss, is ultimately positive.

However, the benefits produced by the filter are very dependent on the location. For the case of Delft, the benefits provided in terms of a lower annual degradation rate did not compensate for the initial optical loss. At this location, the lifetime energy yield of the standard PV module (9,153.57 kWh) was greater than that of the PV module with the thermal filter (8,925.29 kWh). The lifetime of a standard PV module was estimated at 34 years (DR = 0.57%/year). The thermal filter extended this lifetime to 35 years (DR = 0.55%/year). Implementing a thermal filter will cause a relative energy yield loss of 2.49%.

Figure 14b presents the trend of the renormalized power ratio (PR) for the Delft case for both PV modules. The overall results of the degradation study are presented in Table 5. The mean, maximum, and 98th percentile values of operational cell temperature used for the study are those presented in Table 4.

5 | OUTLOOK

The findings of this work indicate that the annual degradation rate can be the critical performance parameter of optimization. This work's main limitation lies in the detachment of the different optimization algorithms,

particularly the second-order optimization stage aimed at improving angular stability while maintaining a simplified structure. Creating a single comprehensive modeling framework that includes this latter algorithm in the overall design would be desirable. The best approach to optimizing the benefit of the optical filter is to find a good balance between τ_0 and DR. τ_0 is proven to be the main driver of optical loss and an essential contributor to lower operational temperature. Therefore, an optimal thermal filter is one whose value of τ_0 optimizes DR such that the DC energy yield lifetime surpasses that of a standard module.

Another important aspect of this work is the selected solar cell architecture. As stated before, the selected IBC solar cell has a specific behavior in the near-infrared wavelength range. Since most of the light at those wavelengths is being either transmitted or reflected, the effect in temperature produced by reflecting in the near-IR range is rather limited. This, however, is different for other c-Si solar cell architectures. On aluminum back surface field (Al-BSF) solar cells, for example, the contribution of the sub-bandgap absorption losses can be significant,[55] leading to operational solar cell temperatures higher than PERC architectures.[48] For Al-BSF cases, a practical design can be focused on only producing rejection on the sub-bandgap range. In general, creating a practical design is dependent on the target cell architecture. The findings produced in this work will be adapted to a wider range of commercially available solar cells in the future.

6 | CONCLUSIONS

This work presented a practical approach to the design of an optical filter that provides passive thermal management to PV modules. The filter was tailored to an IBC solar cell architecture. It was proven that for this architecture, rejection of just IR radiation provides a limited level of thermal management and requires an extremely complex optical filter design.

Therefore, another approach was proposed, consisting of finding a wavelength range that ensures the best reduction of thermalization losses. The simulation framework indicated that a narrow rejection of light on a wavelength range from 400 to 500 nm provided the best cooling potential. It is demonstrated that a practical way to achieve this is to use the harmonic reflection peak created by an optical filter based on the QWOT approach with a design wavelength of λ_0 in the IR region.

The optimization of the optical filter was done by finding, through simulations, the design that provided the lowest optical loss with a reasonable temperature reduction. From an initial design of 11 pairs (p) of SiO_2(L)|SiN_X(H), the value of λ_0 was changed from 1,200 to 1,600 nm. A value of $\lambda_0 = 1{,}350$ nm proved to give the best tradeoff. Later, the number of pairs p was optimized to a value of 4, reducing optical losses without sacrificing the cooling potential significantly. Angular stability was improved using OptiLayer's second-order optimization algorithm, establishing the final number of layers as 15.

Simulating the thermal filter effect on PV modules predicted a cooling potential of 2.20°C for a module located in Delft, NL, and 2.45°C for one located in Singapore. If no degradation effects are accounted for, implementing the thermal filter onto a PV module translates into a DC energy yield loss. For Delft, the relative DC energy yield loss was found to be 10.01%, whereas for Singapore, this value was estimated at 9.76%. The optical losses are not compensated by the cooling provided to the PV module.

However, looking at long-term reliability, the thermal filter extended the lifetime of a PV module by 2 years in Singapore and 1 year in Delft. With degradation effects accounted for, the extended lifetime provided by the thermal filter in Singapore yields an overall positive result in terms of DC energy yield in both scenarios, with relative gains of 3.12%. The benefit provided by the filter is location-dependent, as the overall effect for Delft was still negative, with a relative loss in the lifetime energy yield of 2.49%. Further improvements will be studied in later stages, but this solution ensures reliability and energy yield benefits in hot climates.

TABLE 6 MAE, MBE, and RMSE values for the assessment of the optical model accuracy

	Test filter
MAE	4.25%
MBE	1.49%
RMSE	6.59%

$$0.5L|(HL)^6|H|0.5L \text{ for } \lambda_0 = 1410 \text{ nm}$$
$$L = SiO_2$$
$$H = SiN_X$$

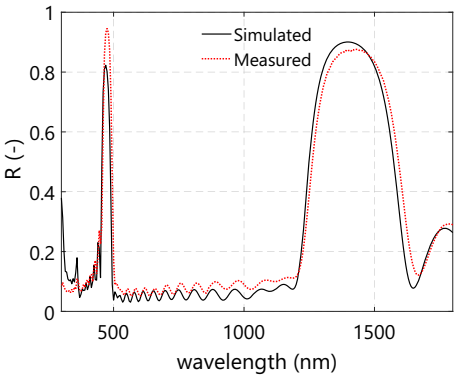

FIGURE 15 The test filter is deposited on glass and measured so that the filter is located on the backside. The resulting filter was measured on a PerkinElmer Lambda device.

7 | EXPERIMENTAL WORK AND MODEL VALIDATION

A test filter was manufactured by plasma-enhanced chemical vapor deposition (PECVD) with a flat glass as a substrate. The size of the glass was 15 cm × 15 cm. The details of the filter layout are found in Figure 15. The coated glass was measured with the filter located at the backside (see Figure 15). The predicted reflectance and the measured reflectance were compared to estimate the error of the optical model. The metrics used to estimate accuracy were the mean bias error (MBE), mean absolute error (MAE), and root mean square error (RMSE).

Table 6 presents the results from the validation procedure. The coated glass was then used as the top layer of a mini-PV module. The module consisted of an encapsulated SunPower Gen II solar cell. Another mini-module, without the thermal filter, was manufactured for comparison. Electrical measurements of both mini-modules were carried out under an AAA solar simulator under STC conditions, obtaining IV curves for both samples. Parameters for electrical simulations were extracted by using the equivalent circuit calculator from PV Lighthouse.[56] The ratio between the measured short circuit current from the mini-module with the filter with respect to its counterpart without the filter was used to scale down the irradiance value of the two-diode electrical model. Results show that this approach is very accurate in predicting the effect of the filter on the electrical performance of the mini-module, as shown in Figure 16a. The electrical model accuracy was assessed by comparing the current values of the generated IV curve via the two-diode model with the measured values, yielding an RMSE value of 0.05 A, as presented in Table 7.

After the electrical measurements, both modules were taken for outdoor temperature measurements. The measurements were carried out for 11 consecutive days. A single T-type thermocouple was placed at the backside of each mini-module, and temperature measurements were taken every 10 s. Both modules were in V_{OC} conditions. Assessment of the thermal model shows that the predicted operating module temperature (backside value) was in very good agreement with the backside measurement, as shown in Figure 16b.

The model predicts the temperature of the backside of a mini-module with a thermal filter with an RMSE value of 1.44°C for the entire range of measured values, as shown in Table 7. The time resolution for this simulation was 20 s to synchronize the temperature data with the measured irradiance data. Application of the thermal model for the case of the standard module produces slightly lower values of MAE, MBE, and RMSE. Figure 17a shows the measured and simulated values for the entire measurement range for this latter case. The difference between these error values of both validations falls within the uncertainty of the measurement sensor (±0.5°C).

The values presented in Table 7, however, are calculated for the entire range of measurements. Analysis of the potential effect on model accuracy of the spectral approach is done by comparing the differences between the prediction of the standard mini-module and the mini-module with the implemented thermal filter. First, the difference between the measured value and the simulated value for each case is defined as

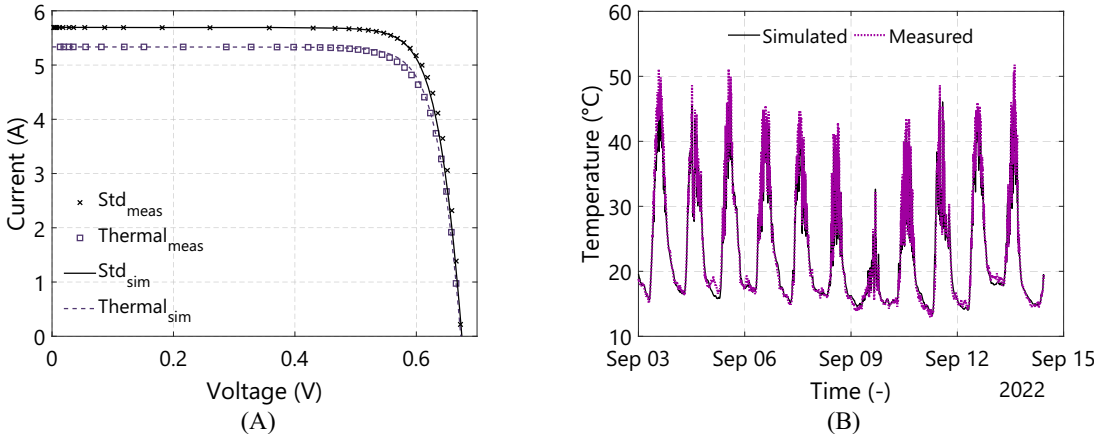

FIGURE 16 (a) Validation of the electrical model for a standard mini-module and a mini-module with a thermal filter. (b) Thermal model validation for 11 consecutive days of measurements of the mini-module equipped with the thermal filter with a time resolution of 10 s

	Electrical model	Thermal model standard	Thermal model filter
MAE	0.03 A	0.87°C	1.00°C
MBE	0.01 A	0.34 °C	0.73°C
RMSE	0.05 A	1.22°C	1.44°C

Note: Numbers in the table refer to the case of a mini-module endowed with the thermal filter.

TABLE 7 Accuracy assessment of the electrical and thermal models used in this work for simulating the thermo-electrical performance of our mini modules

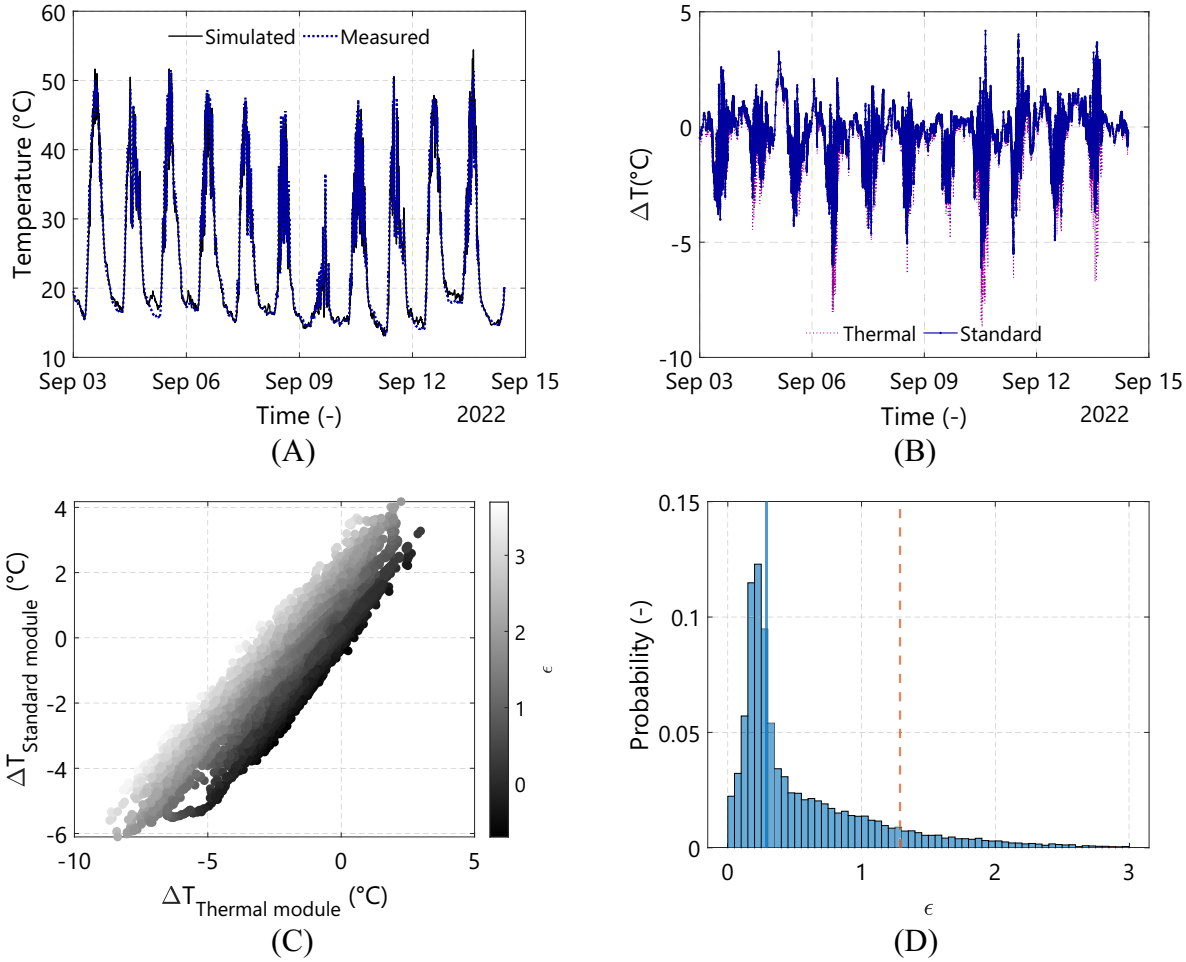

FIGURE 17 (a) Thermal model validation for the case of the standard mini-module for the same period of time and time resolution of the validation presented in Figure 16b. (b) Trends of the difference between the measured value and the predicted value for both mini modules. The trend observed is identical for both mini modules. (c) The analysis of the scatter plot of the parameter ϵ shows a strong correlation of the error between both mini modules, indicating that infrequent high discrepancies occur in both models. (d) Probability histogram of ϵ, showcasing only a marginal difference in the errors obtained on both simulations

$$\Delta T_{module} = T_{measured} - T_{simulated}. \quad (6)$$

Figure 17b shows the same trend for both mini modules. There are, however, differences in the values of ΔT, which sometimes presents greater values for the case of the mini-module with the implemented thermal filter. Estimation of a new parameter, ϵ, defined by Equation (7), enables further analysis:

$$\epsilon = \Delta T_{standard} - \Delta T_{thermal}. \quad (7)$$

Figure 17c indicates that, even though, on occasion, the value of ϵ is greater on the thermal model, the error trend strongly correlates to the error of the standard module. This correlation signifies that a potential error in the model affects both the thermal mini-module and the standard mini-module equally.

The probability histogram of ϵ, presented in Figure 17d, indicates only a marginal deviation of ϵ with a median value of 0.29°C (blue solid line in Figure 17d) and a 90th percentile value of 1.29°C (red dashed line). Therefore, it is unlikely that the infrequent differing values of $\Delta T_{thermal}$ are related to the spectral thermal model.

AUTHOR CONTRIBUTIONS

Juan Camilo Ortiz Lizcano: Writing; coding work; simulation work; experimental work; results analysis. **Ismail Kaaya**: Degradation model coding; degradation simulations; writing; results analysis; revision. **Hesan Ziar**: Results analysis; revision; supervision. **Patricia Seoane da Silva**: Experimental work. **Yilong Zhou**: Experimental work. **Miro Zeman**: Supervision. **Olindo Isabella**: Revision; results analysis; supervision.

ACKNOWLEDGEMENT

The research leading to these results has received funding from the Horizon 2020 Program under Grant Agreement 952957, Trust-PV project.

DATA AVAILABILITY STATEMENT

The data that support the findings of this study are available on request from the corresponding author. The data are not publicly available due to privacy or ethical restrictions.

ORCID

Juan Camilo Ortiz Lizcano https://orcid.org/0000-0002-0165-5493
Hesan Ziar https://orcid.org/0000-0002-9913-2315

REFERENCES

1. Singh P, Ravindra NM. Temperature dependence of solar cell performance—an analysis. *Sol. Energy Mater. Sol. Cells*. 2012;101:36-45. doi:10.1016/j.solmat.2012.02.019
2. Ascencio-Vásquez J, Kaaya I, Brecl K, Weiss KA, Topič M. Global climate data processing and mapping of degradation mechanisms and degradation rates of PV modules. *Energies (Basel)*. 2019;12(24): 4749. doi:10.3390/en12244749
3. Kaaya I, Koehl M, Mehilli AP, de Cardona Mariano S, Weiss KA. Modeling outdoor service lifetime prediction of PV modules: effects of combined climatic stressors on PV module power degradation. *IEEE J. Photovolt.* 2019;9(4):1105-1112. doi:10.1109/JPHOTOV.2019.2916197
4. Kaaya I, Ascencio-Vásquez J, Weiss KA, Topič M. Assessment of uncertainties and variations in PV modules degradation rates and lifetime predictions using physical models. *Solar Energy*. 2021;218(June 2020):354-367. doi:10.1016/j.solener.2021.01.071
5. Gok A, Ozkalay E, Friesen G, Frontini F. The influence of operating temperature on the performance of BIPV modules; the influence of operating temperature on the performance of BIPV modules. *IEEE J. Photovolt.* 2020;10(5):1371-1378. doi:10.1109/JPHOTOV.2020.3001181
6. Amr AAR, Hassan AAM, Abdel-Salam M, El-Sayed AM. Enhancement of photovoltaic system performance via passive cooling: theory versus experiment. *Renew. Energy*. 2019;140:88-103. doi:10.1016/j.renene.2019.03.048
7. Ahmad EZ, Sopian K, Jarimi H, et al. Recent advances in passive cooling methods for photovoltaic performance enhancement. *Int. J. Electr. Comput. Eng.* 2021;11(1):146-154. doi:10.11591/ijece.v11i1.pp146-154
8. Ghadikolaei SSC. Solar photovoltaic cells performance improvement by cooling technology: An overall review. *Int. J. Hydrogen Energy*. 2021;46(18):10939-10972. doi:10.1016/j.ijhydene.2020.12.164
9. Harahap R, Suherman S. Active versus passive cooling systems in increasing solar panel output. *Proc. Environ. Sci. Eng. Manag.* 2021;8(1):157-166.
10. Nižetić S, Giama E, Papadopoulos AM. Comprehensive analysis and general economic-environmental evaluation of cooling techniques for photovoltaic panels, Part II: active cooling techniques. *Energ. Conver. Manage.* 2018;155:301-323. doi:10.1016/J.ENCONMAN.2017.10.071
11. Maghrabie HM, Mohamed ASA, Fahmy AM, Samee AAA. Performance augmentation of PV panels using phase change material cooling technique: a review. *SVU-Int. J. Eng. Sci. Appl.* 2021;2(2):1-13. doi:10.21608/SVUIJESA.2021.87202.1013
12. Ali HM. Recent advancements in PV cooling and efficiency enhancement integrating phase change materials based systems—a comprehensive review. *Solar Energy*. 2020;197. Elsevier Ltd:163-198. doi:10.1016/j.solener.2019.11.075
13. Zhao B, Hu M, Ao X, Xuan Q, Pei G. Spectrally selective approaches for passive cooling of solar cells: a review. *Appl. Energy*. 2020;262:114548. doi:10.1016/j.apenergy.2020.114548
14. Zhu L, Raman A, Wang KX, Anoma MA, Fan S. Radiative cooling of solar cells. *Optica*. 2014;1(1):32. doi:10.1364/optica.1.000032
15. Zhao B, Hu M, Ao X, Pei G. Performance analysis of enhanced radiative cooling of solar cells based on a commercial silicon photovoltaic module. *Solar Energy*. 2018;176:248-255. doi:10.1016/j.solener.2018.10.043
16. Safi TS, Munday JN. Improving photovoltaic performance through radiative cooling in both terrestrial and extraterrestrial environments. *Opt. Express*. 2015;23(19):A1120. doi:10.1364/oe.23.0a1120
17. Zhao B, Hu M, Ao X, Huang X, Ren X, Pei G. Conventional photovoltaic panel for nocturnal radiative cooling and preliminary performance analysis. *Energy*. 2019;175:677-686. doi:10.1016/j.energy.2019.03.106
18. Sato D, Yamada N. Review of photovoltaic module cooling methods and performance evaluation of the radiative cooling method. *Renew. Sustain. Energy Rev.* 2019;104(July 2018):151-166. doi:10.1016/j.rser.2018.12.051
19. Hu M, Zhao B, Ao X, et al. Applications of radiative sky cooling in solar energy systems: Progress, challenges, and prospects. *Renew. Sustain. Energy Rev.* 2022;160:112304. doi:10.1016/j.rser.2022.112304
20. Khorrami N, Rajabi Zargarabadi M, Dehghan M. A novel spectrally selective radiation shield for cooling a photovoltaic module. *Sustain Energy Technol Assess*. 2021;46(April):101269. doi:10.1016/j.seta.2021.101269
21. Vaillon R, Dupré O, Cal RB, Calaf M. Pathways for mitigating thermal losses in solar photovoltaics. *Sci. Rep.* 2018;8(1):13163. doi:10.1038/s41598-018-31257-0
22. Sun X, Silverman TJ, Zhou Z, Khan MR, Bermel P, Alam MA. An optics-based approach to thermal management of photovoltaics: selective-spectral and radiative cooling. *IEEE J. Photovolt.* 7(2):566-574.
23. Heideier RB, Gimenes ALV, Udaeta MEM, Saidel MA. Optical filter design applied to photovoltaic modules to maximize energy production. *Solar Energy*. 2018;159:908-913. doi:10.1016/j.solener.2017.10.013
24. Lu Y, Chen Z, Ai L, et al. A universal route to realize radiative cooling and light management in photovoltaic modules. *Solar RRL*. 2017;1(10):1700084. doi:10.1002/solr.201700084
25. Lin S, Ai L, Zhang J, et al. Silver ants-inspired flexible photonic architectures with improved transparency and heat radiation for photovoltaic devices. *Sol. Energy Mater. Solar Cells*. 2019;203:110135. doi:10.1016/j.solmat.2019.110135
26. Cui X, Sun X, Zhou L, Wei X. Thermal and electrical performance analysis of monofacial double-glass photovoltaic module with radiative cooling coating on the rear surface. *Solar Energy*. 2023;264:111986. doi:10.1016/j.solener.2023.111986
27. Ingenito A, Luxembourg S, Spinelli P, Weeber A, Isabella O, Zeman M. Optimized metal free back reflectors for high efficiency open rear c-Si solar cells. In: *2015 IEEE 42nd Photovoltaic Specialist Conference, PVSC 2015*. Institute of Electrical and Electronics Engineers Inc.; 2015. doi:10.1109/PVSC.2015.7356157
28. Isabella O, Dobrovolskiy S, Kroon G, Zeman M. Design and application of dielectric distributed Bragg back reflector in thin-film silicon solar cells. *J. Non Cryst. Solids*. 2012;358(17):2295-2298. doi:10.1016/j.jnoncrysol.2011.11.025
29. Ortiz Lizcano JC, Villa S, Zhou Y, et al. Optimal Design of multilayer optical color filters for building-integrated photovoltaic (BIPV) applications. *Solar RRL*. 2023;7(19):2300256. doi:10.1002/solr.202300256
30. Bläsi B, Kroyer T, Kuhn TE, Höhn O. The MorphoColor concept for colored photovoltaic modules. *IEEE J. Photovolt.* 2021;11(5):1305-1311. doi:10.1109/JPHOTOV.2021.3090158
31. Xu Z, Matsui T, Matsubara K, Sai H. Tunable and angle-insensitive structural coloring of solar cell modules for high performance building-integrated photovoltaic application. *Sol. Energy Mater. Sol. Cells*. 2022;247:111952. doi:10.1016/j.solmat.2022.111952

32. Adachi L, Hanashi G, Kubota S, et al. Highly efficient color-control technique for building-integrated photovoltaics using optical dielectric thin film. *Jpn. J. Appl. Phys.* 2023;62(SL):SK1010. doi:10.35848/1347-4065/acc594
33. Isabella O. *Light Management in Thin-Film Silicon Solar Cells*. Delft University of Technology; 2013.
34. An Y, Sheng C, Li X. Radiative cooling of solar cells: Opto-electro-thermal physics and modeling. *Nanoscale*. 2019;11(36):17073-17083. doi:10.1039/c9nr04110a
35. Akerboom E, Veeken T, Hecker C, van de Groep J, Polman A. Passive radiative cooling of silicon solar modules with photonic silica microcylinders. *ACS Photonics*. 2022;9(12):3831-3840. doi:10.1021/acsphotonics.2c01389
36. Zhao B, Hu M, Ao X, Xuan Q, Pei G. Comprehensive photonic approach for diurnal photovoltaic and nocturnal radiative cooling. *Sol. Energy Mater. Sol. Cells*. 2018;178:266-272. doi:10.1016/j.solmat.2018.01.023
37. Perrakis G, Tasolamprou AC, Kenanakis G, Economou EN, Tzortzakis S, Kafesaki M. Combined nano and micro structuring for enhanced radiative cooling and efficiency of photovoltaic cells. *Sci. Rep.* 2021;11(1):11552. doi:10.1038/s41598-021-91061-1
38. Perrakis G, Tasolamprou AC, Kenanakis G, Economou EN, Tzortzakis S, Kafesaki M. Passive radiative cooling and other photonic approaches for the temperature control of photovoltaics: a comparative study for crystalline silicon-based architectures. *Opt. Express*. 2020;28(13):18548-18565. doi:10.1364/oe.388208
39. Fan G, Duan B, Zhang Y, Li X, Ji X. Full-spectrum selective thin film based photonic cooler for solar cells of space solar power station. *Acta Astronaut.* 2021;180:196-204. doi:10.1016/j.actaastro.2020.12.035
40. Slauch IM, Deceglie MG, Silverman TJ, Ferry VE. Spectrally selective mirrors with combined optical and thermal benefit for photovoltaic module thermal management. *ACS Photonics*. 2018;5(4):1528-1538. doi:10.1021/acsphotonics.7b01586
41. Li W, Shi Y, Chen K, Zhu L, Fan S. A comprehensive photonic approach for solar cell cooling. *ACS Photonics*. 2017;4(4):774-782. doi:10.1021/acsphotonics.7b00089
42. Ortiz Lizcano JC, Procel P, Calcabrini A, et al. Colored optic filters on c-Si IBC solar cells for building integrated photovoltaic applications. *Progr. Photovolt. Res. Appl.* 2022;30(4):401-435. doi:10.1002/PIP.3504
43. Gueymard CA. The SMARTS spectral irradiance model after 25 years: new developments and validation of reference spectra. *Sol. Energy*. 2019;187:233-253. doi:10.1016/J.SOLENER.2019.05.048
44. Santbergen R, Meguro T, Suezaki T, Koizumi G, Yamamoto K, Zeman M. GenPro4 optical model for solar cell simulation and its application to multijunction solar cells. *IEEE J. Photovolt.* 2017;7(3):919-926. doi:10.1109/JPHOTOV.2017.2669640
45. Tikhonravov AV, Trubetskov MK. Development of the needle optimization technique and new features of OptiLayer design software. *Opt. Interf. Coat.* 1994;2253(November 1994):10. doi:10.1117/12.192109
46. Power Advantage, "Maxeon ™ GEN II SOLAR CELLS MAXEON ™ GEN II SOLAR CELLS electrical characteristics of a typical Maxeon Gen II Cell," pp. 3–4, 2013.
47. Ristau D, Ehlers H, Thin film optical coatings 2012. 10.1007/978-3-642-19409-2_6.
48. Vogt MR, Schulte-Huxel H, Offer M, et al. Reduced module operating temperature and increased yield of modules with PERC instead of Al-BSF solar cells. *IEEE J. Photovolt.* 2017;7(1):44-50. doi:10.1109/JPHOTOV.2016.2616191
49. Seoane da Silva P, "Infrared optical filters for passive cooling of c-Si solar modules," Delft University of Technology, Delft.
50. Tikhonravov AV. Needle optimization technique: the history and the future. *Optical Thin Films V. New. Dev.* 1997;3133:2. doi:10.1117/12.290180
51. Tikhonravov AV, Trubetskov MK, DeBell GW. Optical coating design approaches based on the needle optimization technique. *Appl. Optics*. 2007;46(5):704-710. doi:10.1364/AO.46.000704
52. Trubetskov MK, Tikhonravov A v. Modern design tools and a new paradigm in optical coating design. *Appl. Optics*. 2012;51(30):7319-7332. doi:10.1364/AO.51.007319
53. Šúri M, Huld TA, Dunlop ED. PV-GIS: a web-based solar radiation database for the calculation of PV potential in Europe. *Int. J. Sustain. Energy*. 2005;24(2):55-67. doi:10.1080/14786450512331329556
54. Kaaya I, Alzade A, Tuomiranta A, Ascencio-Vásquez J, Saelens D, Gordon I, "Lifetime prediction of photovoltaic modules: towards a generalized physics-based approach," in 8th World Conference on Photovoltaic Energy Conversion, Milan, 2022.
55. Xu L, Liu W, Liu H, et al. Heat generation and mitigation in silicon solar cells and modules. *Aust. Dent. J.* 2021;5(3):631-645. doi:10.1016/j.joule.2021.01.012
56. PV Lighthouse, "PV lighthouse: equivalent-circuit calculator." Accessed: Oct 21, 2022. [Online]. Available: https://www.pvlighthouse.com.au
57. Vogt MR, Hahn H, Holst H, et al. Measurement of the optical constants of soda-lime glasses in dependence of iron content and modeling of iron-related power losses in crystalline si solar cell modules. *IEEE J. Photovolt.* 2016;6(1):111-118. doi:10.1109/JPHOTOV.2015.2498043
58. Vogt MR, Holst H, Schulte-Huxel H, et al. Optical constants of UV transparent EVA and the impact on the PV module output power under realistic irradiation. *Energy Procedia*. 2016;92:523-530. doi:10.1016/J.EGYPRO.2016.07.136
59. Aly SP, Ahzi S, Barth N, Figgis BW. Two-dimensional finite difference-based model for coupled irradiation and heat transfer in photovoltaic modules. *Sol. Energy Mater. Sol. Cells*. 2018;180:289-302. doi:10.1016/J.SOLMAT.2017.06.055
60. Deceglie MG, Nag A, Shinn A, et al., RdTools version: 2.2.0-beta.1. 2023. doi:10.5281/zenodo.7411201, https://github.com/NREL/rdtools
61. Macleod HA. *Thin-film optical filters*. 5th ed. CRC Press; 2017:696 pages. doi:10.1201/b21960

How to cite this article: Lizcano JCO, Kaaya I, Ziar H, et al. Practical design of an optical filter for thermal management of photovoltaic modules. *Prog Photovolt Res Appl*. 2024;32(11):753-773. doi:10.1002/pip.3813

APPENDIX A: OPTICAL PROPERTIES OF THE DIFFERENT MATERIALS CONSIDERED IN THIS WORK

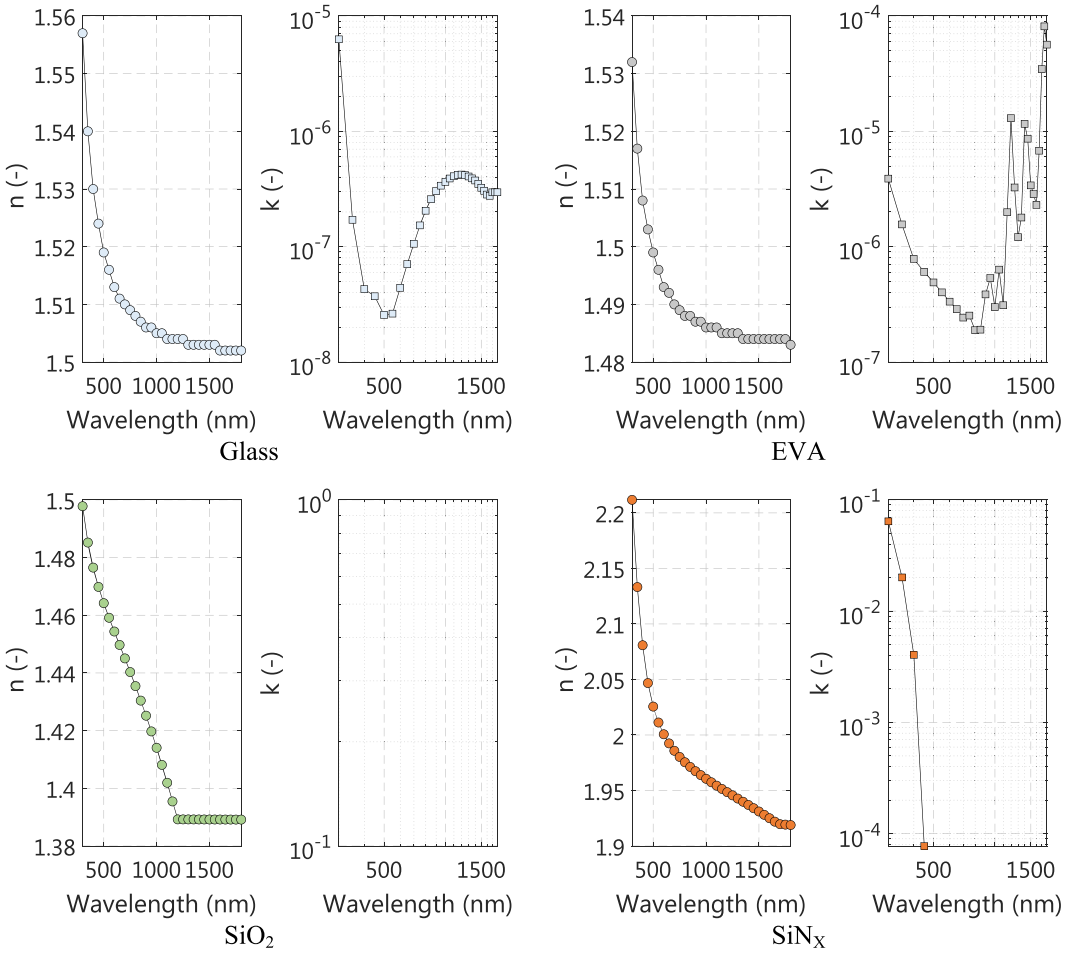

FIGURE A1 Optical properties used in this work for glass (data obtained from Vogt et al.[57]), ethyl vinyl acrylate (EVA, with data obtained from Vogt et al.[58]), silicon oxide, and silicon nitride (data obtained from measurements on a glass substrate via spectroscopic ellipsometry)

A.1 | Physical and thermal properties used in this work

Table A1 describes the thickness and the thermal properties of the different materials employed in the modeled PV module. Thermal data are obtained from Aly et al.[59]

A.2 | Additional details on the optical, thermal, and electrical modeling

The modeling framework estimates the spectral plane of array irradiance for every time instant. The spectrum is estimated based on the

TABLE A1 Physical and thermal properties of the different materials considered in the model of the PV module[59]

Layer	Thickness—*d* (m)	Thermal conductivity—*k* (W/m K)	Density—ρ (kg/m^3)	Specific heat capacity—C_p (J/kg K)
Glass	3.2×10^{-3}	1.8	3,000	500
EVA (x 2)	580×10^{-6}	0.35	960	2,090
PV Cell	210×10^{-6}	148	2,330	677
Back sheet	100×10^{-6}	0.2	1,200	1,250

air mass using SMARTS (see Figure A2). The GenPro4 software models the PV module's optical system based on each layer's optical properties, as described in Figure A1. Spectral values of reflectance (R), transmittance (T), and absorptance (A) are estimated for each layer of the module for angles of incidence of light ranging from 0° (normal incidence) to 87° with a resolution of 3°. Using these values of R, T, and A, the scaling factors described in Equations (1) and (2) are calculated, which in turn allows the estimation of G_{cell} (Equation 3).

The spectral plane of array irradiance and the absorptance values estimate the volumetric heat produced within the module (see Figure A3), thus estimating T_{cell}. All the mathematical details can be found in Ortiz Lizcano et al.[42] and Aly et al.[59]

Using both G_{cell} and T_{cell} as inputs, a two-diode model provides the electrical output of a single solar cell. The parameters used in this model were extracted using the measured JV curve of a single solar cell and PV lighthouse's calculator (see Table A2).[56]

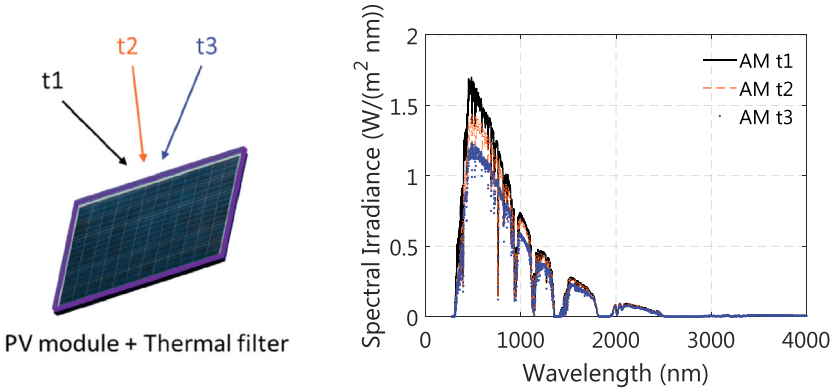

FIGURE A2 Estimation of the spectral plane of array irradiance for each time instant is done by calculating the air mass and modeling a spectrum based on clear skies using SMARTS. The spectrums are normalized and then multiplied by the respective scalar values of each irradiance component, which are calculated using the Perez Model and weather data obtained from Meteonorm

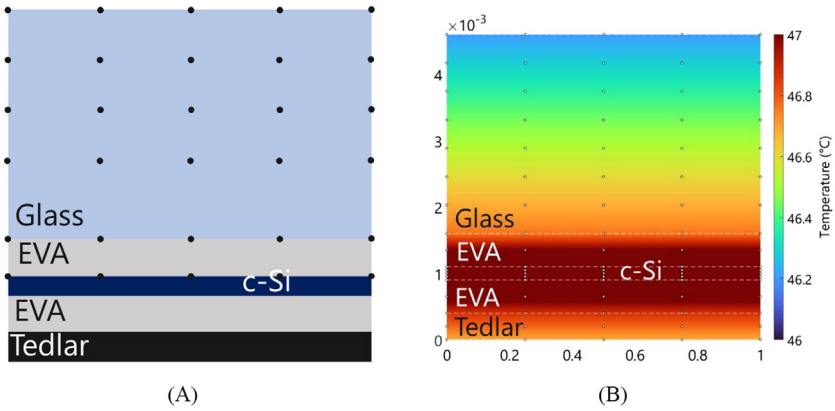

FIGURE A3 (a) The PV module is divided into finite volumes represented by nodes. At each node, the appropriate heat transfer mechanisms are used to obtain a temperature profile like the one shown in (b).

TABLE A2 Two diode parameters used in this work

Parameter	Symbol	Unit	Value
Light collected current	(J_L)	(mA/cm^2)	37.204
Saturation current 1	(J_1)	(pA/cm^2)	0.14
Ideality factor 1	(m_1)	(–)	1
Saturation current 2	(J_2)	(nA/cm^2)	3.74
Ideality factor 2	(m_2)	(–)	2
Shunt resistance	(R_{SH})	(kΩ cm^2)	18
Series Resistance	(R_S)	(Ω cm^2)	0.6

Note: The values were found using the calculator from PV Lighthouse.[56]

APPENDIX B: DETAILS OF THE OPTICAL FILTERS USED IN THIS WORK

TABLE B1 Near ideal IR optical filter from Figure 2a

Material	Thickness (nm)
MgF_2	71.786
TiO_2	12.115
MgF_2	14.143
TiO_2	103.513
MgF_2	9.596
TiO_2	24.217
MgF_2	31.757
TiO_2	12.008
MgF_2	206.884
TiO_2	8.805
MgF_2	43.425
TiO_2	21.54
MgF_2	25.762
TiO_2	29.313
MgF_2	6.916
TiO_2	133.606
MgF_2	13.158
TiO_2	23.62
MgF_2	39.08
TiO_2	7.792
MgF_2	200.468
TiO_2	14.456
MgF_2	23.749
TiO_2	104.132
MgF_2	11.274
TiO_2	17.22
MgF_2	24.399
TiO_2	7.899
MgF_2	184.479
TiO_2	8.588
MgF_2	42.585
TiO_2	21.777
MgF_2	18.303
TiO_2	32.811
MgF_2	5.328
TiO_2	143.184
MgF_2	13.315
TiO_2	24.662
MgF_2	35.75
TiO_2	10.169
MgF_2	189.375
TiO_2	6.726
MgF_2	18.704
TiO_2	11.621
MgF_2	13.452
TiO_2	109.145
MgF_2	22.992
TiO_2	11.938
MgF_2	195.57
TiO_2	12.967
MgF_2	23.1
TiO_2	105.362
MgF_2	22.859
TiO_2	13.366
MgF_2	192.455
TiO_2	13.099
MgF_2	23.413
TiO_2	102.046
MgF_2	23.67
TiO_2	14.987
MgF_2	183.67
TiO_2	9.799
MgF_2	11.723
TiO_2	6.734
MgF_2	14.9
TiO_2	98.307
MgF_2	17.149
TiO_2	7.326
MgF_2	11.924
TiO_2	8.551
MgF_2	178.002
TiO_2	10.698
MgF_2	25.996
TiO_2	14.618
MgF_2	6.851
TiO_2	91.923
MgF_2	16.756
TiO_2	18.438
MgF_2	39.163
TiO_2	6.556
MgF_2	186.103

Note: Final design of the thermal filter that was used for all the performance and degradation calculations. The layers are not in the order of deposition but rather in the order of how light travels through the filter once it goes through the front glass.

TABLE B2 Thickness values and order of layers of the optimized filter that provides the optical performance presented in Figure 12b and 12d.

Material	Thickness (nm)
SiO_2	103
SiN_X	163
SiO_2	226
SiN_X	176
SiO_2	67
SiN_X	16
SiO_2	125
SiN_X	169
SiO_2	258
SiN_X	16
SiO_2	23
SiN_X	151
SiO_2	33
SiN_X	17
SiO_2	208

Note: Notice that, to replicate the behavior shown in Figure 12b, the filter needs to be simulated working within the complete optical system described Figure 5 (i.e., considering the entire PV module layout).

APPENDIX C: ANNUAL DEGRADATION RATE—OTHER IMPORTANT RESULTS

The degradation rate from the simulated time series was evaluated using the year-on-year (YOY) method based on NREL Rdtools,[60] as shown in Figure C1. Both temperature and irradiance corrections are considered in the evaluations. The irradiance filter of 200–1,200 W/m^2 is used to remove nighttime data and non-uniform irradiance scenarios.

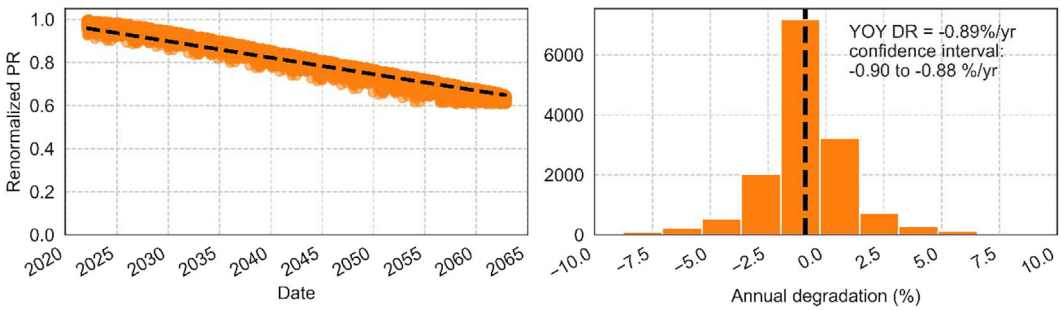

FIGURE C1 (Left) Evolution of daily renormalized daily performance ratio (PR) (dashed line is a linear fit) and (right) the corresponding histogram of the annual degradation rate (DR) based on the YOY analysis (dashed line shows the median)